



# Boost antimicrobial effect of CTAB-capped $\text{Ni}_x\text{Cu}_{1-x}\text{O}$ ( $0.0 \leq x \leq 0.05$ ) nanoparticles by reformed optical and dielectric characters

Basit Ali Shah<sup>1,2,\*</sup>, Bin Yuan<sup>1,\*</sup> , Yu Yan<sup>1</sup>, Syed Taj Ud Din<sup>2</sup>, and Asma Sardar<sup>3</sup>

<sup>1</sup> School of Materials Science and Engineering, South China University of Technology (SCUT), Guangzhou 510640, People's Republic of China

<sup>2</sup> Faculty of Basic and Applied Sciences (FBAS), School of Physics, International Islamic University Islamabad (IIUI), Islamabad, Pakistan

<sup>3</sup> Department of Chemistry, Hazara University Mansehra, Dhodial, Pakistan

Received: 17 January 2021

Accepted: 23 April 2021

Published online:

11 May 2021

© The Author(s), under exclusive licence to Springer Science+Business Media, LLC, part of Springer Nature 2021

## ABSTRACT

Chemical doping and coating have been considered as efficient semiconductor physics strategies to modulate the physical, chemical, and biological properties of materials for the required applications. In this study, cetyltrimethylammonium bromide (CTAB) stabilizer-capped nickel-doped cupric oxide ( $\text{Ni}_x\text{Cu}_{1-x}\text{O}$ ) nanoparticles (NPs) with different doping concentrations ( $0.0 \leq x \leq 0.05$ ) were synthesized via a one-step rapid and low-cost solvothermal synthesis route. The as-synthesized CTAB-capped  $\text{Ni}_x\text{Cu}_{1-x}\text{O}$  NPs have been sightseen for their structural/morphological, optical/dielectric, and antimicrobial properties using XRD/SEM/TEM, FT-IR/UV-visible/Impedance spectroscopies, and Agar well diffusion method, respectively. Relevant results show enhanced optical, dielectric and antimicrobial properties with Ni doping due to the smaller size effect. Importantly, in vitro examination, the antimicrobial activity of the grown NPs was evaluated against four microbial species, exhibits that the CTAB-capped Ni-doped CuO NPs possess a command antimicrobial toxicity to *Staphylococcus aureus* (25923-ATCC), *Klebsiella pneumoniae* (700603-ATCC), and *Escherichia coli* (25922-ATCC) and an intermediate performance towards *Candida albicans* (24433-ATCC). The minimum inhibitory concentration (MIC) assay for the obtained CTAB- $\text{Ni}_{0.05}\text{Cu}_{0.95}\text{O}$  sample upon *S. aureus* or *K. pneumoniae* pathogens reaches extremely as low as  $5 \mu\text{g ml}^{-1}$  for all reported CuO NPs. The improved dose-dependent antimicrobial effect has been found to be strongly dependent on the particle size, surface morphology, elemental compositions, and surface bio-functionality of the catalytic nanomaterials. Additionally, Ni-

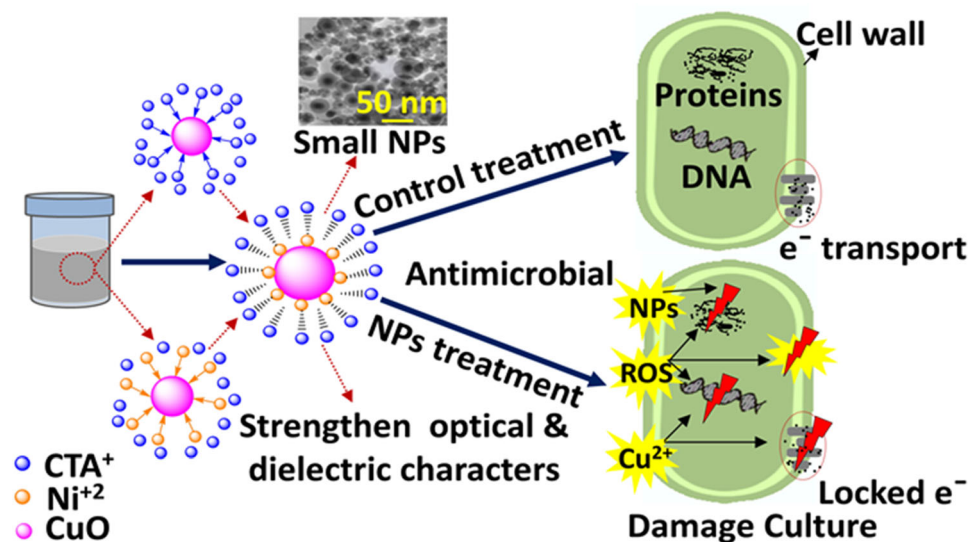
Handling Editor: Yaroslava Yingling.

Address correspondence to E-mail: basitalimrz@gmail.com; apsheng@scut.edu.cn

<https://doi.org/10.1007/s10853-021-06130-7>

dopant, CTAB-stabilizer, and binding of  $\text{Cu}^+/\text{Cu}^{2+}$  ions with respiratory enzymes collectively produce an excess amount of reactive oxygen species (ROS) in the bacterial culture medium, which determines a predominant antibacterial mechanism for bacterial cells damage. Overall, these inorganic ( $\text{Ni}_x\text{Cu}_{1-x}\text{O}$ ) NPs with antimicrobial cationic surfactant (CTAB) have advantages to use as a functionalized disinfection nanoagent to control the microbial infections in the healthcare sector together with various electronic and photonic medical diagnoses.

## GRAPHICAL ABSTRACT



## Introduction

Nanotechnology is continuously developing new approaches and directions to monitor, repair, and control human biological systems, even at a molecular scale. Nanomedicine development has recently attracted much research interest and became an urgent requirement for biomedical and pharmaceutical applications [1]. This is because the ineffectiveness of traditional medications, together with high bacterial resistance, has raised a serious concern to the healthcare sector. Studies from the world health organization (WHO) revealed that multidrug-resistant (MDR) pathogens such as *Klebsiella pneumoniae*, *Staphylococcus aureus*, *Escherichia coli*, and *Candida albicans* are causing a very high percentage of

common healthcare infections [2, 3]. According to one survey, only a single MRSA (methicillin-resistant staphylococcus aureus)-resistant organism kills too many peoples every year than HIV's/AID's or Parkinson's diseases [4]. MDR pathogens, including VRE (vancomycin-resistant enterococci), CREB (carbapenem-resistant enterobacteriaceae), and KPC (klebsiella pneumoniae carbapenemase), etc., are other serious risks of emerging resistant microbes to almost every market available antibiotic [5]. As a proof of concept, research has been declared that more than 80% wide variety of microbial infections in the body is caused by biofilms [6, 7]. It has been proposed that pathogen growth in such biofilms responds to oxidative stress, which not only induces biofilms formation but also secretes a lot of

extracellular polymeric substances (EPSs) [8]. These EPSs destroy non-competent cells causing the release of DNA, polypeptides, and polymeric carbohydrates, etc., in the surrounding medium, developing a mature biofilm that demonstrates tolerance toward antibiotics and the host immune system [8, 9]. Infections associated with the bacterial biofilms are more challenging to eradicate by traditional antibiotics, while advanced and effective disinfection drugs development is necessary for the delicacy of biofilms infections [9, 10]. A minimal number of effective antimicrobial drugs are employed for many decades that treat the microbial infections. Inevitably, it is crucial to control the virulent bacterial strains using facile synthetic strategies to develop novel antimicrobial disinfectants with enhanced antimicrobial and antibiofilm activity. In recent years, plenty of nanomaterials have been explored as novel antimicrobial agents against different clinically isolated microbes [11, 12]. Among them, ionic nanoparticulate transition metal oxides (TMOs) exhibit numerous distinct benefits in reduced acute toxicity, less particle aggregation rate, as well as overwhelming the existing antibiotic resistance [13]. On the other hand, several research reports revealed that the particle size, shape, specific surface area, roughness, doping, and coatings, etc., are the most critical factors that significantly influence the antimicrobial activity of the TMOs [14–16]. Additionally, depending on the synthesis technique, the studies revealed that low-dimensional nanomaterials present higher antibacterial efficacy than the bulk high-dimensional materials, based on their optical, electrical, and fluorescence intensity [17, 18].

In this context, copper oxide (CuO) nanoparticles with modified physical properties and unusual crystalline structure with reactive sites have been recommended as a suitable choice for dose-dependent antimicrobial activity applications [19–21]. These compounds have potential to kill harmful bacteria and viruses and inhibit biofilm pathogens' functionality [22–24]. However, the high surface areas and increased electron–hole recombination rate resulting in aggregated bulk CuO NPs limiting their bactericidal performance. During past decades, many strategies have been developed for enhancing the therapeutic efficacy of CuO NPs. Among them, CuO has been doped by an appropriate amount of other transition metals (TMs) such as Fe [25], Ni [26], Ag [22], Zn [27], and so on [28], as well as coated with

cationic surfactants [29] that prevents the aggregation of NPs indicating the easiest way to alter their physical, chemical, and biological properties. For instance, the optical band gap energy has been found to increase by increasing Ni-dopant concentrations reported by Ansari et al. in the Ni-doped CuO [30]. The promoted optical and electrical properties of Ni-incorporated CuO nanoparticles are reported by Baturay et al. [31]. Basith and co-workers explored the Ni doping-induced effect on band gap and magnetic properties of CuO [32]. The impact of TMs doping on optical and magnetic assets of the neat CuO was also investigated and used as an antibacterial agent against various MDRs microbes in Ref. [33]. Another report on improved optical and antibacterial properties was presented by Ramya et al. for Ni<sup>2+</sup> ion-enriched CuO nanoparticles [34]. And there are many reports available on correlated properties of different elements-doped CuO [35–38]. To make better use of CuO NPs against different MDR pathogens, we report the effect of Ni-doping and CTAB-coating on CuO NPs which prevents the aggregation of the NPs, resulting excellent antimicrobial performance followed by improved optical and dielectric characters. The dielectric and antimicrobial properties of the metals-doped CuO are rarely considered and yet to be examined. However, the antimicrobial performance against various MDR pathogens of these reported CuO NPs is still not satisfied for real applications. The development of nanomaterials with reformed optical and dielectric functionalities in medical and pharmaceutical fields may be significantly conducive for the treatment of microbial infections.

In this regard, an effort has been made to tune the optical, dielectric, and antimicrobial properties of CuO via nickel (Ni) doping with the assistance of antimicrobial cationic surfactant (cetyltrimethylammonium bromide, CTAB), using a facile and cost-effective solvothermal synthesis route. The substitution of Ni elements into the CuO matrix together with CTAB-stabilizer capping has drastically increased the optical band gap, dielectric property, and AC electrical conductivity of the products, debating a crucial role as antimicrobial agents against various MDR microbes. By increasing the Ni element doping into the CTAB-CuO NPs leads to lattice strain and electronic structure modification, which substantially increase the ROS production through resulting best bactericidal performance toward pathogenic bacterial

strains, namely *Staphylococcus aureus* (25923-ATCC), *Klebsiella pneumoniae* (700603-ATCC), and *Escherichia coli* (25922-ATCC) as well as intermediate antifungal activity against *Candida albicans* (24433-ATCC).

## Experimental

### Materials and characterizations

All chemical reagents, copper(II) chloride di-hydrate ( $\text{CuCl}_2 \cdot 2\text{H}_2\text{O}$ ), Nickel(II) chloride penta-hydrate ( $\text{NiCl}_4 \cdot 5\text{H}_2\text{O}$ ), cetyltrimethylammonium bromide (CTAB), Oleylamine (OAm), and hexane were used of analytical grade and purchased from Sigma-Aldrich (China). Ethanol and OAm were used as reaction media. The bacterial species used in this work are *E. coli* (25922-ATCC), *K. pneumoniae* (700603-ATCC), *S. aureus* (25923-ATCC), and *C. albicans* (24433-ATCC). These microorganisms were collected from the Microbiology department of Hazara University, Mansehra, Pakistan. These four isolates are MDRs and usually cause several human diseases in our daily lives [39]. The protein content and catalase activity in the four microbial strains were carried using an Enzyme-labeled instrument (ELIASA) by Varioskan LUX (Thermo Fisher Scientist, USA), which is a previously described protocol [28]. A high-resolution X-ray diffractometer (XRD) in ( $20^\circ$ – $80^\circ$ ) 2-theta scale with Cu-K $\alpha$  radiations of wavelength ( $\lambda = 0.154056$  nm) was used for structural analysis. Morphologies and structures were characterized using a scanning/transmission electron microscope (SEM/TEM), respectively. An energy-dispersive spectroscopy (EDS) attached to SEM was used to confirm the samples' chemical compositions. UV-visible spectra were acquired using a quartz slab spectrophotometer (Perkin Elmer Lambda 25-UV). FTIR-spectrometer (Nexus-870) in the spectral range of  $380$ – $4000$   $\text{cm}^{-1}$  wavenumbers was operated using the KBr thin pellets method to obtain FT-IR spectra. The dielectric parameters and AC conductivity were analyzed using an LCR (inductance–capacitance–resistance) meter (7600 + IET Labs) at room temperature ( $24 \pm 2$  °C).

### Synthesis of CTAB-Ni<sub>x</sub>Cu<sub>1-x</sub>O NPs

CTAB-capped Ni<sub>x</sub>Cu<sub>1-x</sub>O ( $0.0 \leq x \leq 0.05$ ) NPs were synthesized using a facile and economical

solvothermal synthesis technique, as shown in the schematic diagram of Fig. 1. In a typical experiment, 0.1 M of copper chloride di-hydrate ( $\text{CuCl}_2 \cdot 2\text{H}_2\text{O}$ ) and appropriate amounts of nickel chloride penta-hydrate ( $\text{NiCl}_4 \cdot 5\text{H}_2\text{O}$ ) were dissolved into 10 ml Oleylamine (OAm) at room temperature ( $24 \pm 2$  °C) to obtain pure and Ni (1, 3 and 5 Molar. %)–doped CuO homogenous suspension. Then 0.1 M of cetyltrimethylammonium bromide (CTAB) was utterly dissolved into 20 ml Ethanol and slowly added into the above running solution under constant magnetic stirring. The obtained suspension was transferred into a 50 ml quartz line Teflon reactor and heat-treated at 100 °C for 40 min first and subsequently heated to 200 °C for 90 min with a ramp rate of  $2.5$  °C  $\text{min}^{-1}$ , respectively. The synthesis in the presence of CTAB and OAm as capping surfactants and Ethanol as hydrolysis play crucial role in controlling size and shape of the CuO NPs. After, naturally cool down to room temperature, a black precipitate was assembled by centrifuge and rinsed several times using an ethanol and hexane mixed solvent (2:1). Finally, the obtained precipitates were vacuum-dried at 70 °C for 3 h to get the samples.

### Antimicrobial susceptibility testing (AST)—Agar well diffusion method

The antimicrobial susceptibility test (AST) of the prepared samples was screened using a well-known Agar well diffusion protocol [40]. Four pathogenic *S. aureus* (25923-ATCC), *K. pneumoniae* (700603-ATCC), *E. coli* (25922-ATCC), and *C. albicans* (24433-ATCC) strains were used as test microbes. Before bacterial suspension preparation, all experimental tools were sterilized in an open air microwave oven at 110 °C for an hour. The direct colony suspension method was used to prepare inoculums of the test bacteria in the nutrient agar and swabbed the Mueller Hinton agar (MHA) plates with each pathogenic bacterial strain's resultant saline suspension. The density of each bacterial suspension was adjusted to  $1.5 \times 10^8$  CFU  $\text{ml}^{-1}$  by 0.5 McFarland standard. The wells were bored into each nutrient agar plate using a 6-mm cork borer. Each sample's stock suspension was prepared in deionized water at varying concentrations of  $0$   $\mu\text{g ml}^{-1}$ ,  $5$   $\mu\text{g ml}^{-1}$ ,  $15$   $\mu\text{g ml}^{-1}$ ,  $30$   $\mu\text{g ml}^{-1}$ ,  $45$   $\mu\text{g ml}^{-1}$ , and  $60$   $\mu\text{g ml}^{-1}$  by mixing them with nutrient agar media to assess the antimicrobial liability of NPs. The  $0$   $\mu\text{g ml}^{-1}$  concentration represents the control group

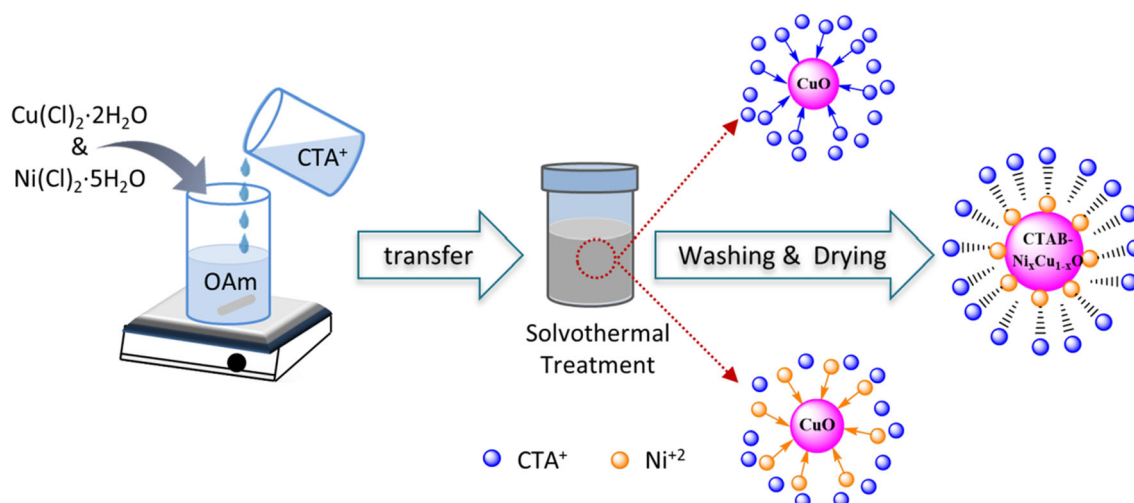


**Figure 1** Stepwise schematic diagram for the preparation of CTAB-assisted  $\text{Ni}_x\text{Cu}_{1-x}\text{O}$  nanoparticles.

for experiment—a suspension containing no nanoparticles. In the last 40  $\mu\text{L}$  of the prepared antimicrobial suspensions were added to each well. The resulting plates were left for half an hour before being incubated on a rotary machine (nearly 170 revolutions per minute) at 37  $^\circ\text{C}$  for 18 h. After the incubation process, a perfect diameter of the zone for bacterial growth inhibition was determined even at a low dose. The determinations were done in duplicate. The obtained zone diameter of each sample was interpreted with the comparative study of CLSI (clinical laboratory of the standard institute) criteria.

### Determination of minimum inhibitory concentration (MIC)

Before determination of the minimum inhibitory concentration (MIC) for each sample, the 96-well microtiter plates were cleaned with ethanol to avoid any kind of experimental contamination. After that, the first sixth rows are filled with 40  $\mu\text{L}$  nutrient agar containing  $\sim 1.5 \times 10^8$  cfu  $\text{ml}^{-1}$  of each microbial culture with different concentrations (0, 5, 15, 30, 45 and 60  $\mu\text{g ml}^{-1}$ ) of each antimicrobial compound. The wells of the seventh row till the eleventh are pipetted with 40  $\mu\text{L}$  of respective individual antimicrobial compound mixed with few drops of nutrient agar media. The top most row of well containing nutrient agar media and individual microbial culture but without (0  $\mu\text{g ml}^{-1}$ ) concentration of antimicrobial compound is adopted as the control for the experiment. The rest of rows which contain on nutrient agar and antimicrobial agents but without

bacterial culture are termed as blank control for the experiment. After incubation aerobically at 37  $^\circ\text{C}$  for 18 h, the samples are scanned using microplate photometer. The MIC value is the lowest dilution of the compound in the nutrient agar medium that causes the growth inhibition of the test microbes.

### Statistical analysis

The obtained biological results are statistically analyzed using Microsoft Excel 2010 software. All experiments were performed in duplicate and the mathematical average (Means  $\pm$  STD) of the set of data were analyzed by Excel sheet formulas. The antimicrobial effect of CTAB-capped  $\text{Ni}_x\text{Cu}_{1-x}\text{O}$  ( $0.00 \leq x \leq 0.05$ ) NPs with respect to varying concentrations (0, 5, 15, 30, 45 and 60  $\mu\text{g ml}^{-1}$ ) against Gram + Ve (*S. aureus* (25923-ATCC), *C. albicans* (24433-ATCC)) and Gram -Ve (*K. pneumoniae* (700603-ATCC), *E. coli* (25922-ATCC)) pathogenic species are evaluated and compared with the control group.

### Results and discussion

The XRD patterns of the well-grown CTAB-capped  $\text{Ni}_x\text{Cu}_{1-x}\text{O}$  NPs with varying doping concentration ( $x = 0.00, 0.01, 0.03$  and  $0.05$ ) are demonstrated in Fig. 2a. It can be seen that all diffraction peaks are well indexed to (110),  $(\bar{1}11)/(002)$ , (111)/(200),  $(\bar{2}02)$ , (020), (202),  $(\bar{1}13)$ ,  $(\bar{3}11)$ , (220), (311) and (004) crystallographic planes appearing at 32.4°, 35.5°, 38.6°,

48.8°, 53.3°, 58.1°, 61.5°, 66.1°, 67.9°, 72.4°, and 75.0° of  $2\theta$  angles, respectively, indicating a single-phase monoclinic structure of CuO with  $C_2/c$  space group, confirmed from the reported JCPDS card # 05-0661 of CuO. There is no extra peak assigned to the impurity phase of Ni, Cu, or other possible secondary phases like NiO and Cu<sub>2</sub>O, etc., observed in the XRD results, ensure the formation of targeted Ni, Cu, and O containing compounds. Further the extended view of the recorded double-reflections ( $\bar{1}11$ )/(002) and (111)/(200) crystallographic planes (Fig. 2b) identified broadening in the characteristic peaks together with a slight peak shift (0.072°–0.26°) toward higher angles of  $2\theta$  values with the increase of Ni doping concentration ( $x$ ) resulting strains in the lattice parameters. In this perspective, Ni substitution exhibits a pronounced effect on the crystallite size, unit cell

volume, and other lattice parameters of the CuO which are consistent with the results obtained by Al-Amri et al. [31] and Dwivedi et al. [41] in Ni-doped CuO NPs. The crystallite size ( $D$ ) for all prepared samples is determined by fitting Debye Scherrer's formula as follows [42].

$$D = \frac{0.9\lambda}{t \cos\theta} \quad (1)$$

where  $\lambda$ ,  $t$ , and  $\theta$  represents the wavelength of Cu-K $\alpha$  radiations (0.15407 nm), FWHM (Full width half maximum) of the characteristic diffraction patterns of ( $\bar{1}11$ )/(002) and (111)/(200) crystallographic planes and diffraction Bragg's angle in degree, respectively. The calculated average crystallite size of the CTAB-capped Ni <sub>$x$</sub> Cu<sub>1- $x$</sub> O samples are 22.53 ± 1.23 nm (for  $x = 0.00$ ), 20.87 ± 1.25 nm (for  $x = 0.01$ ), 18.34 ± 1.00 nm (for  $x = 0.03$ ), and 16.58 ± 0.91 nm

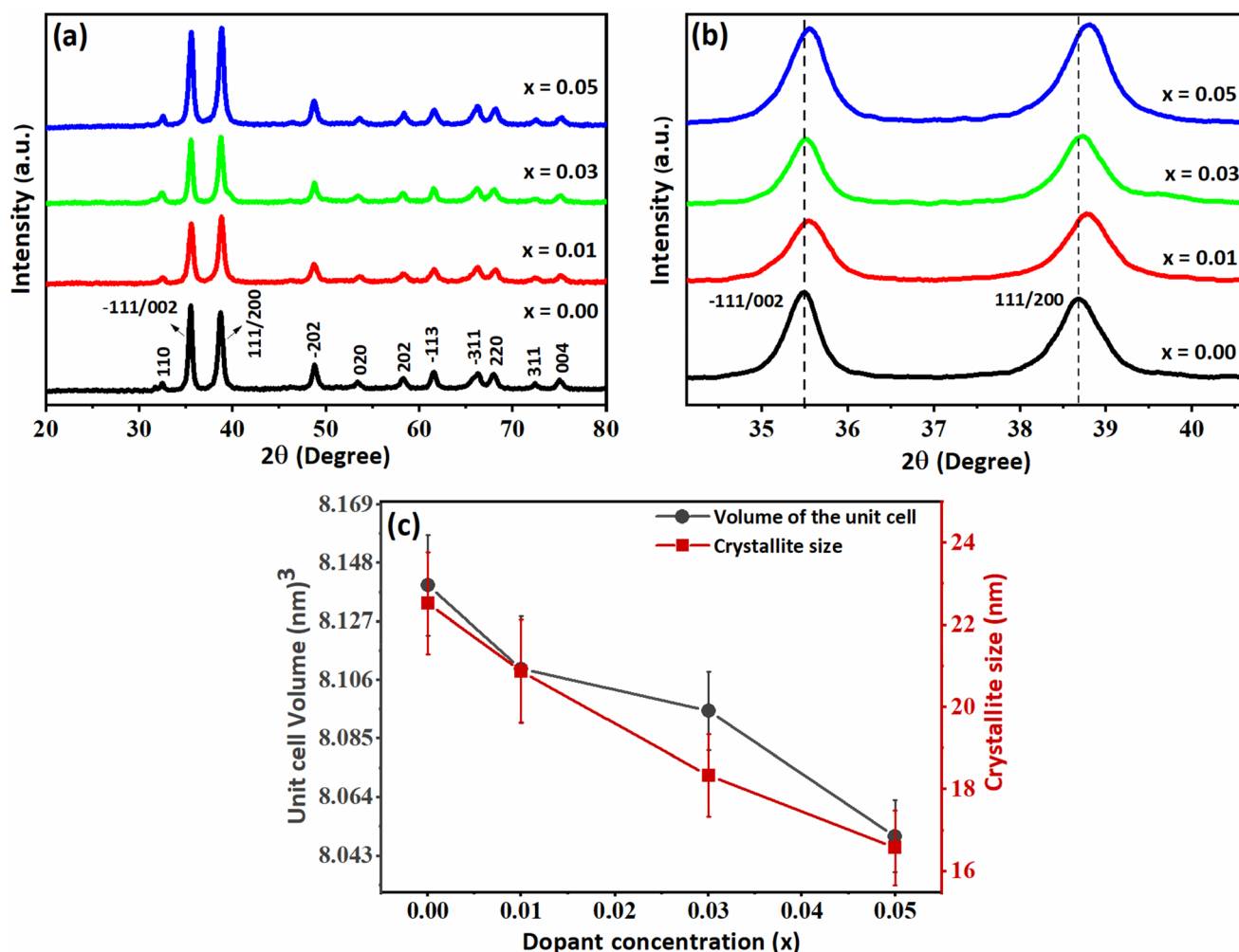


**Figure 2** X-ray diffraction patterns (a) Extended view of the peaks shift (b) and variation in crystallite size (red) and unit cell volume (gray) (c) of the CTAB- Ni <sub>$x$</sub> Cu<sub>1- $x$</sub> O ( $x = 0.00, 0.01, 0.03$  and  $0.05$ ) samples.

(for  $x = 0.05$ ), respectively. The reduction in crystallite size ( $D$ ) with the increase of dopant concentration ( $x$ ) is shown in Fig. 2c. The substitution of  $\text{Ni}^{2+}$  ions in the host  $\text{CuO}$  lattice creates stress due to the difference in ionic radii that cause grain growth inhibition, indicating a decrease in the crystallite size and other lattice parameters. The lattice parameters ( $a$ ,  $b$ , and  $c$ ) are calculated from the interplanar distance ( $d$ ) derived from the Bragg's equation and followed by Miller ( $hkl$ ) indices, using the following relation [43].

$$\frac{1}{d^2} = \frac{1}{\sin^2\beta} \left( \frac{h^2}{a^2} + \frac{k^2}{b^2} \sin^2\beta + \frac{l^2}{c^2} - \frac{2hl}{ac} \cos\beta \right) \quad (2)$$

where  $\beta$  represents the interfacial unit cell angle, which is equal to  $99.54^\circ$  [44]. The obtained lattice constants  $a = 0.4696$  nm,  $b = 0.3430$  nm,  $c = 0.5129$  nm for CTAB- $\text{Ni}_x\text{Cu}_{1-x}\text{O}$  ( $x = 0.00$ ) sample are slightly greater than that of the average value of  $x = 0.01$  ( $a = 0.4706$  nm,  $b = 0.3416$  nm,  $c = 0.5121$  nm),  $x = 0.03$  ( $a = 0.4708$  nm,  $b = 0.3406$  nm,  $c = 0.5125$  nm) and  $x = 0.05$  ( $a = 0.4670$  nm,  $b = 0.3412$  nm,  $c = 0.5123$  nm) samples. The decrease in the lattice constants of the doped samples creates lattice strain since the ionic radius of the  $\text{Ni}^{2+}$  (0.069 nm) dopant is smaller than the substituted  $\text{Cu}^{2+}$  (0.071 nm) ion. The lattice strain ( $\epsilon$ ) is calculated from the broadening of the characteristic peaks using the following equation [45].

$$\epsilon = \frac{1}{\sin\theta} \left( \frac{\lambda}{D} - t \cos\theta \right) \quad (3)$$

The observed lattice strains in the samples show increasing trend with the increase in doping concentration ( $x$ ), which may be attributed to the broadening in the X-ray diffraction peaks, thereby reducing the lattice constants of the unit cell. This phenomenon was also reported by Mallika et al. [46] in Mg-substituted ZnO nanoparticles. Table 1 depicts the obtained structural parameters for all prepared samples, demonstrating that the crystallite size decreases as the dopant concentration increases, which may be due to the slight difference in correlated ionic radii of the replacing ( $\text{Ni}^{2+}$ ) and replaced ( $\text{Cu}^{2+}$ ) ions. According to Vegard's rule, the substitution of an ion with the smaller size than the host ion leads to the lattice parameters' contraction, thereby decreasing the unit cell volume [47]. The unit cell volume ( $V$ ) and X-rays density ( $\rho_{x\text{-ray}}$ ) are derived using the following equations [43, 48].

$$V = abc \sin\beta \quad (4a)$$

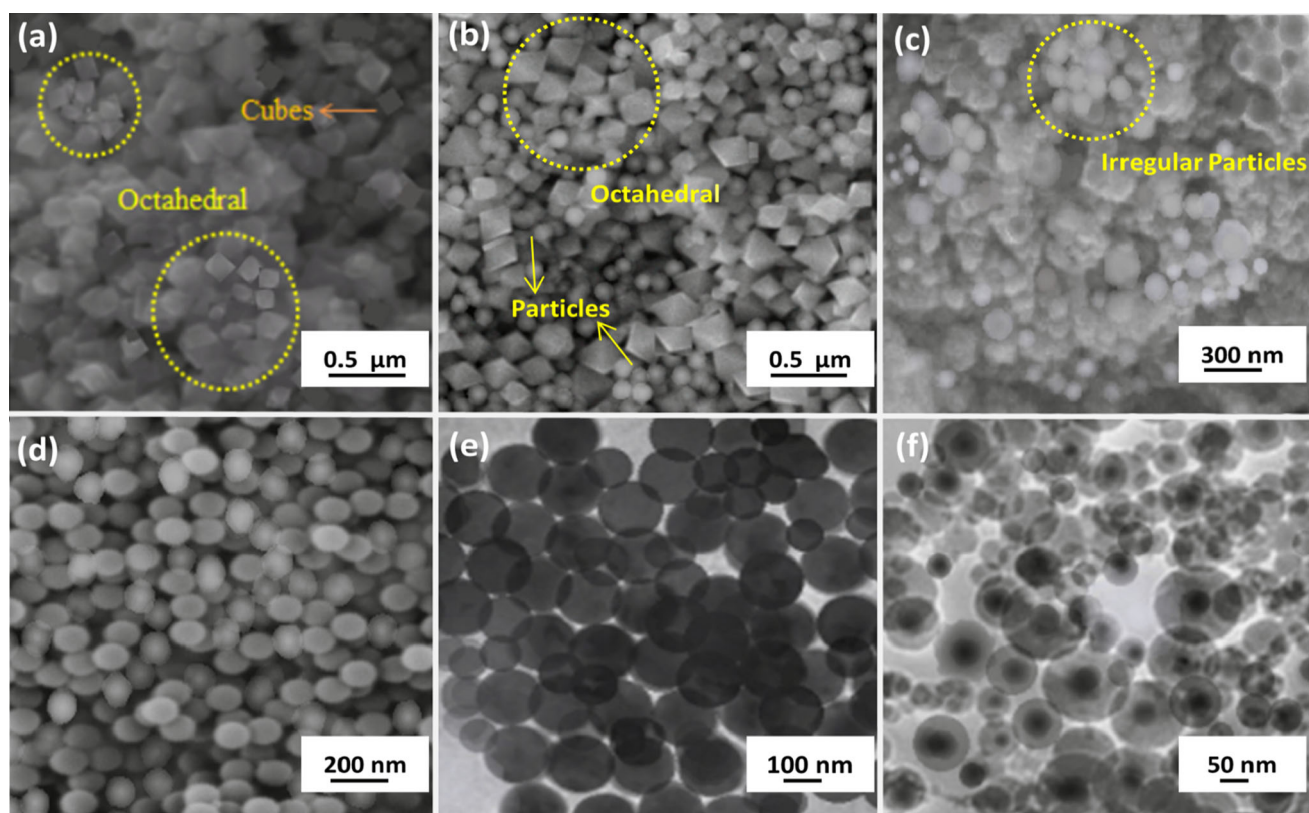
$$\rho_{x\text{-ray}} = \frac{ZM_w}{N_a V} \quad (4b)$$

where  $Z$  denotes molecule numbers per unit cell,  $M_w$  is the molecular weight, and  $N_a$  is the Avogadro's number. The volume of the unit cell ( $V$ ) and molecular weight ( $M_w$ ) are the two key variables that significantly affecting the X-ray density ( $\rho_{x\text{-ray}}$ ) of the products. The presented data in Table 1 shows decreasing of  $\rho_{x\text{-ray}}$  value with Ni element doping ( $x$ ), due to the smaller unit cell volume ( $V$ ) and molecular weight ( $M_w$ ) of the doped samples than the neat  $\text{CuO}$  sample. These outcomes confirm the successful substitution of  $\text{Ni}^{2+}$  in the host  $\text{CuO}$  lattice, indicating contraction in the lattice constants, volume of the unit cell, and crystallite size, as illustrated in Fig. 2c.

The distinctive morphology and shape of the well-grown nanostructures are shown in Fig. 3a–f. Most of the observed particles for pure CTAB-capped  $\text{CuO}$  sample are agglomerated octahedral, except a few cubes crystals with random orientation, as illustrated in Fig. 3a. After varying Ni doping concentrations ( $x$ ), the initial morphology of the undoped sample modifies to mixed spherical and octahedral structures (for  $x = 0.01$ ), irregular diffused particles (for  $x = 0.03$ ) and fine spherical particles (for  $x = 0.05$ ) with a reduction in the particle size as shown in Fig. 3b–d, respectively. The diffused structures may be due to the large surface area of the nanoscale samples. Typically, the mixed and diffused morphology is observed in many cases during nanoparticle synthesis [32, 33, 49, 50]. The variation in the morphology and a decrease in particle nature with Ni doping suggests that the atomic volume of  $\text{Ni}^{2+}$  ( $6.59 \text{ cm}^3 \text{ mol}^{-1}$ ) is smaller than the  $\text{Cu}^{2+}$  ( $7.1 \text{ cm}^3 \text{ mol}^{-1}$ ) element. In other words, grain boundaries pinning by particle effect take place due to the Ni elements doping, say the stress is preventing the grain growth, which resulted in reduced grain size [51, 52]. In short, the effective capping of CTAB and Ni doping significantly reduces the surface tension and aggregation of the  $\text{CuO}$  NPs, resulting in fine spherical particles for the sample ( $x = 0.05$ ). Figure 3e and f present the TEM bright field and dark field images of the prepared  $\text{Ni}_{0.05}\text{Cu}_{0.95}\text{O}$  sample to visualize the CTAB dispersion state and morphology of the NPs. They confirm CTAB capping of  $\text{Ni}_{0.05}\text{Cu}_{0.95}\text{O}$  NPs with good colloidal dispersion stability. The well-

**Table 1** XRD-derived parameters of the synthesized CTAB-Ni<sub>x</sub>Cu<sub>1-x</sub>O (0.0 ≤ x ≤ 0.05) NPs

Sample	Interplanar distance (nm) d <sub>(002)</sub> , d <sub>(200)</sub> , d <sub>(020)</sub>	Lattice constant (nm) a, b, c	Unit cell angle β (°)	Average crystallite size (nm) ± SD	FWHM (t)	Micro-strain (10 <sup>-3</sup> )	Unit cell volume (nm <sup>3</sup> )	X-ray density (g/cm <sup>3</sup> )
CTAB-CuO	0.2527, 0.2314, 0.1715	0.4696, 0.3430, 0.5129	99.552	22.53 ± 1.239	0.3337	1.97	8.140 ± 0.018	6.413
CTAB-Ni <sub>0.01</sub> Cu <sub>0.99</sub> O	0.2523, 0.2319, 0.1708	0.4706, 0.3416, 0.5121	99.574	20.87 ± 1.252	0.3606	2.16	8.110 ± 0.019	6.389
CTAB-Ni <sub>0.03</sub> Cu <sub>0.97</sub> O	0.2525, 0.2320, 0.1703	0.4708, 0.3406, 0.5125	99.589	18.34 ± 1.007	0.4103	2.21	8.095 ± 0.014	6.347
CTAB-Ni <sub>0.05</sub> Cu <sub>0.95</sub> O	0.2523, 0.2301, 0.1706	0.4670, 0.3412, 0.5123	99.615	16.58 ± 0.913	0.4539	2.29	8.050 ± 0.013	6.286

**Figure 3** SEM images of the CTAB-Ni<sub>x</sub>Cu<sub>1-x</sub>O (x = 0.00, 0.01, 0.03 and 0.05) nanoparticles (a–d) TEM bright field and dark field images of the CTAB-Ni<sub>x</sub>Cu<sub>1-x</sub>O (x = 0.05) nanoparticles (e, f).

identified nanoparticles without aggregated bulk particles indicate the effective capping of cationic CTAB on the grown NPs. Sui et al. [53] reported that

the use of cationic surfactant (CTAB) during nano-materials synthesis develops a CTAB-bilayer on materials surface, which significantly increases their



colloidal stability. The chemical composition and elemental percentage in the prepared samples are confirmed using EDS analysis, as depicted in Fig. 4a–d. The EDS spectra reveal the high quality of expected elemental compositions (C, Cu, O, and Ni) without any related impurity in the grown CTAB-Ni<sub>x</sub>Cu<sub>1-x</sub>O samples. The peak due to carbon is assigned to the CTA<sup>+</sup> coating on the CuO and Ni-doped CuO. The obtained data from EDS analysis also indicate that the atomic/weight percentage of the Cu decreases as the concentrations of Ni-doping increases which confirms the successful incorporation of Ni in the host CuO matrix.

FTIR technique is used to evaluate the presence of functional groups to study the phase purity and lattice alterations in the given samples. Figure 5a shows the FT-IR plots of freshly prepared CTAB-stabilized Ni<sub>x</sub>Cu<sub>1-x</sub>O (*x* = 0.00, 0.01, 0.03, and 0.05) NPs in the spectral range of 380–4000 cm<sup>-1</sup> wavenumbers, indicating the vibrational modes of different functional groups. The first three characteristic bands seemed at 413 cm<sup>-1</sup>, 493 cm<sup>-1</sup>, and 608 cm<sup>-1</sup> correspondings to Cu–O stretching vibration along (202)

direction indicating the formation of CuO. The band at 493 cm<sup>-1</sup> could be a representative stretching Cu–O bond, which is further assigned to the B<sub>2u</sub> vibrational mode of the monoclinic structure of CuO [54]. Thangamani et al. [55] have already reported the stretching vibrations at 433, 505, and 610 cm<sup>-1</sup> which confirms the Cu–O phase of the CuO nanostructures. The two bands located at 835 cm<sup>-1</sup> and 1385 cm<sup>-1</sup> can be attributed to the O–H deformation and symmetric stretching vibration of the carboxylate groups. The wide absorption band that appeared at 1639 cm<sup>-1</sup> is attributed to the bending vibration mode of the H–O–H group, and the bands located at 3115 cm<sup>-1</sup> and 3325 cm<sup>-1</sup> are assigned to the stretching vibration of the O–H group. The bending and stretching vibrational bands are due to the adsorbed moisture during pallets of samples preparation for FTIR analysis. The absorption peak near 2368 cm<sup>-1</sup> corresponds to a vibrational C–H stretching band originating from cationic surfactant CTAB use during sample preparation. These assignments are in good agreement with the reported literature elsewhere [55–58]. It is noteworthy that the non-

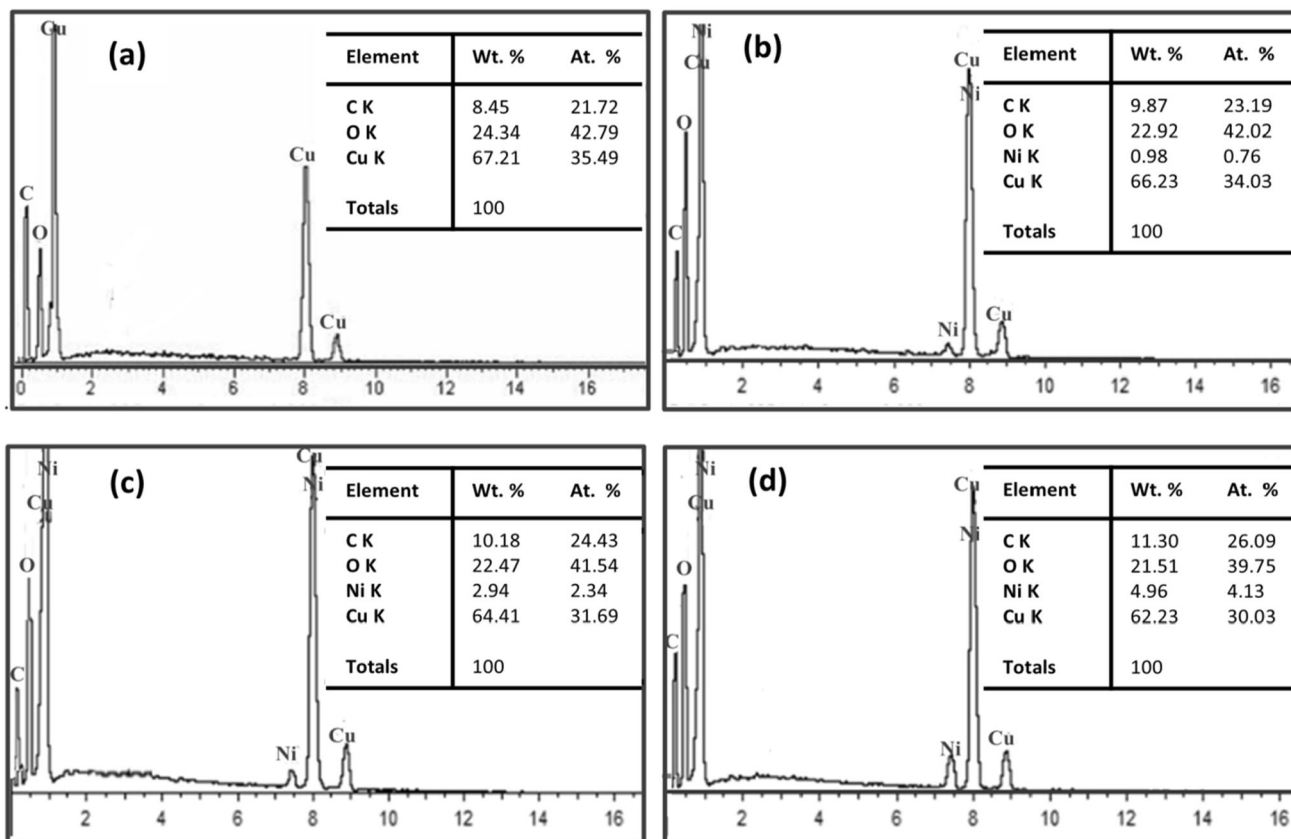
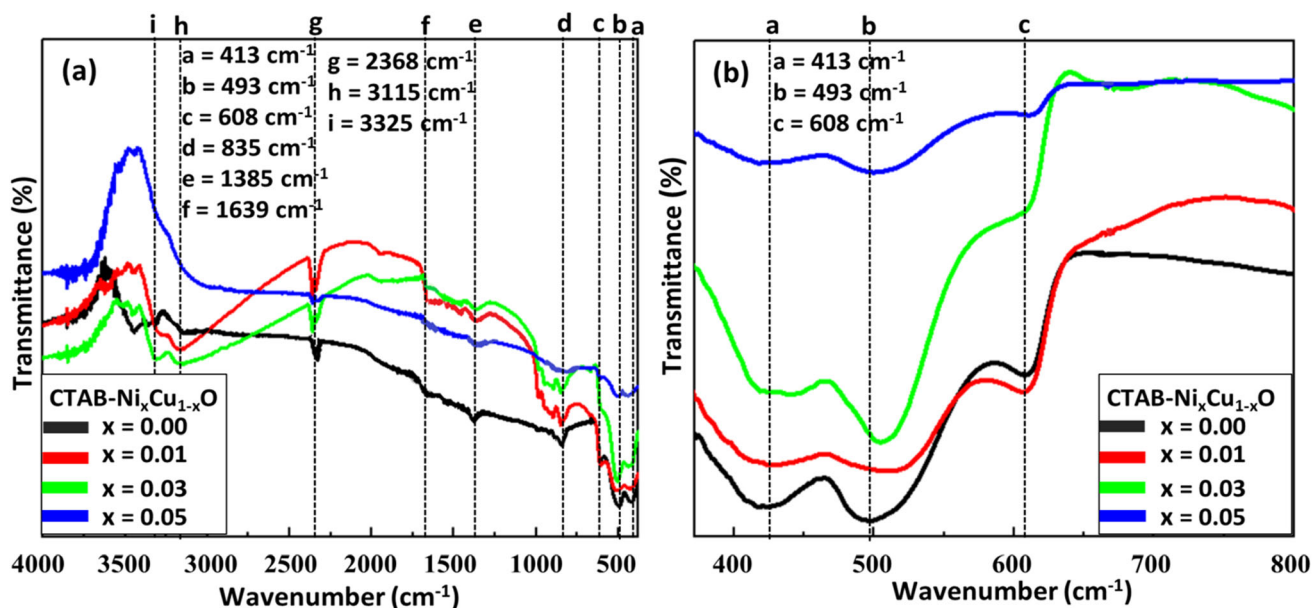


Figure 4 a–d EDS spectra of the CTAB-Ni<sub>x</sub>Cu<sub>1-x</sub>O (*x* = 0.00, 0.01, 0.03, and 0.05) nanoparticles.



**Figure 5** FTIR spectra **a** Extended view recorded in 380–800  $\text{cm}^{-1}$  range **b** of the CTAB- $\text{Ni}_x\text{Cu}_{1-x}\text{O}$  ( $x = 0.00, 0.01, 0.03,$  and  $0.05$ ) samples.

existence of secondary phases associated with the vibrational modes like  $\text{Cu}_2\text{O}$  or  $\text{Ni-O}$ , etc., again confirms the purity and high quality of the reported NPs. Also, the extended view of Fig. 5b depicts a slight shift and broadening in the intensity of the characteristic peaks with the increase of Ni doping concentration ( $x$ ), indicating a variation in the bond length of Cu, Ni, and O elements which confirms the successful substitution of  $\text{Ni}^{2+}$  in the host  $\text{CuO}$  matrix with a decrease in the grain size. Zhang et al. reported similar peaks shift and broadening with a reduction in crystallite size in Ref [59]. These results are concerning with the obtained XRD results of the prepared samples.

To further investigate the influence of Ni doping on the electronic band gap of the  $\text{CuO}$  NPs using UV–visible absorption spectra as depicted in Fig. 6a. It can be seen that the UV–visible absorption spectra for all  $\text{Ni}_x\text{Cu}_{1-x}\text{O}$  ( $0.00 \leq x \leq 0.05$ ) samples exhibit a broad absorption edge ranging from UV to visible light region of the electromagnetic spectrum. Maximum absorbance is recorded at 321 nm for  $x = 0.00$ , which is slightly shifted toward lower wavelengths such as 318 nm, 314 nm, and 309 nm for  $x = 0.01, 0.03,$  and  $0.05$  samples, respectively. This shift toward lower wavelength indicates an increase in the energy gap due to the synthesized NPs' quantum size effect

which is already observed in many cases [32, 60, 61]. This blue shift behavior can be explained by Burstein–Moss bandgap-filling effect, which is mostly observed in n-type semiconductors [62, 63]. According to this effect, when the carrier concentration increases, the Fermi energy level shift close to the conduction band, and the low energy transition is blocked, due to which the band gap energy increases. The absorption optical band gap energy ( $E_g$ ) of the NPs can be calculated using the appropriate Tauc's relation [64].

$$(\alpha h\nu)^n = A(h\nu - E_g) \quad (5)$$

where  $E_g$  denotes the optical band gap energy,  $\nu$  is the vibrational frequency,  $A$  and  $h$  represent the proportionality and Planck's constants,  $\alpha$  is the absorption function, and  $n = 2$  or  $1/2$  indicates direct or indirect allowed band transition. The energy band ( $E_g$ ) can also be determined by plotting a graph between  $(\alpha h\nu)^n$  and  $h\nu$  variables using UV–visible absorption spectra. Draw the tangent line from the linear portion of the curve to a minimum of the Y-axis to get the expected value of the energy band, as shown in Fig. 6b. The calculated band gap energies of the CTAB- $\text{Ni}_x\text{Cu}_{1-x}\text{O}$  NPs for  $x = 0.00$  are 2.00 eV and it is increased to 2.16 eV, 2.34 eV, and 2.49 eV as increasing the doping concentration ( $x$ ) to 0.01, 0.03, and 0.05, respectively. The obtained band gap values

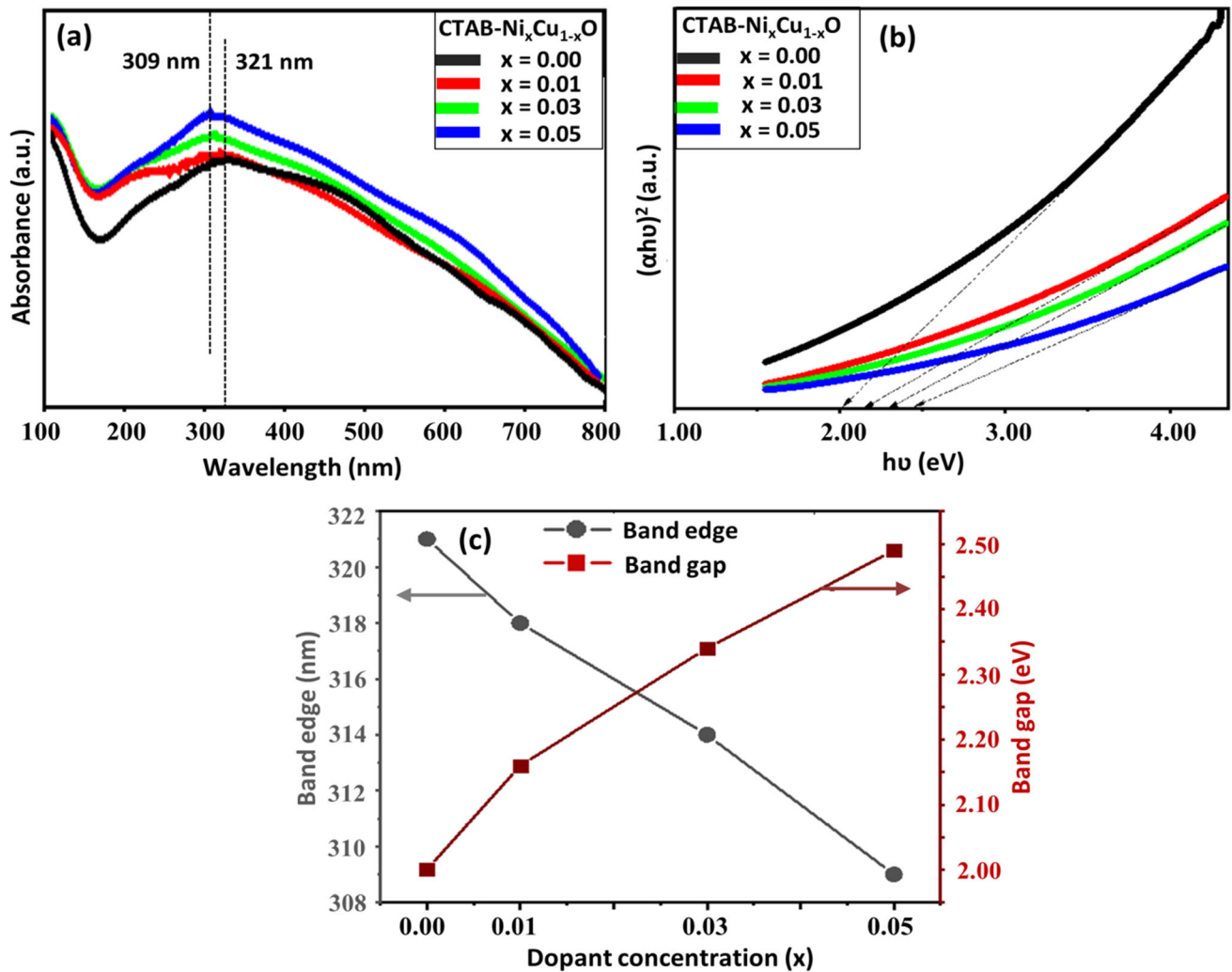


**Figure 6** UV–visible absorption spectra (a) Optical band gap energies (b) and variation in absorption band edge (gray) and band gap (red) as a function of dopant concentration  $x$  (c) for all prepared samples.

exist between 2.00 and 2.49 eV, which are higher than the bulk CuO band gap ( $E_g = 1.86$  eV) [65]. Figure 6c depicts the comparative study of widening in the optical band gap and a reduction in the UV–visible absorption edge with the addition of Ni content ( $x$ ), demonstrating a reduction in the crystallite size of CuO. The increased band gap represents the formation of smaller size nanoparticles, which modifies the products’ AC electrical conductivity, resulting in the release of electrons that interact with the microbial cells that produce reactive oxygen species (ROS) by offering command toxicity to targeted microbes [22].

The electrical behavior of the prepared samples is investigated using an LCR-meter in a wide range of frequency (1 Hz to 2 MHz) at room temperature

( $24 \pm 2$  °C). It can be seen in Fig. 7 that the dielectric constant, loss tangent, and AC electrical conductivity of the neat CuO sample show variation with applied field frequency and dopant concentrations ( $x$ ). The high dielectric constant ( $\epsilon'$ ) for all samples decreases slowly in the low-frequency regions and achieves almost a constant value at higher frequencies. The dielectric decrement behavior can be explained in terms of Maxwell’s Weigner model [66, 67]. According to this model, it is assumed that there are well-conducting grains inside the materials disconnected from each other by resistive grain boundaries. When the external electric field is applied, the mobile charge carriers inside materials quickly accumulate at the grains’ interfaces but do not cross the grain-

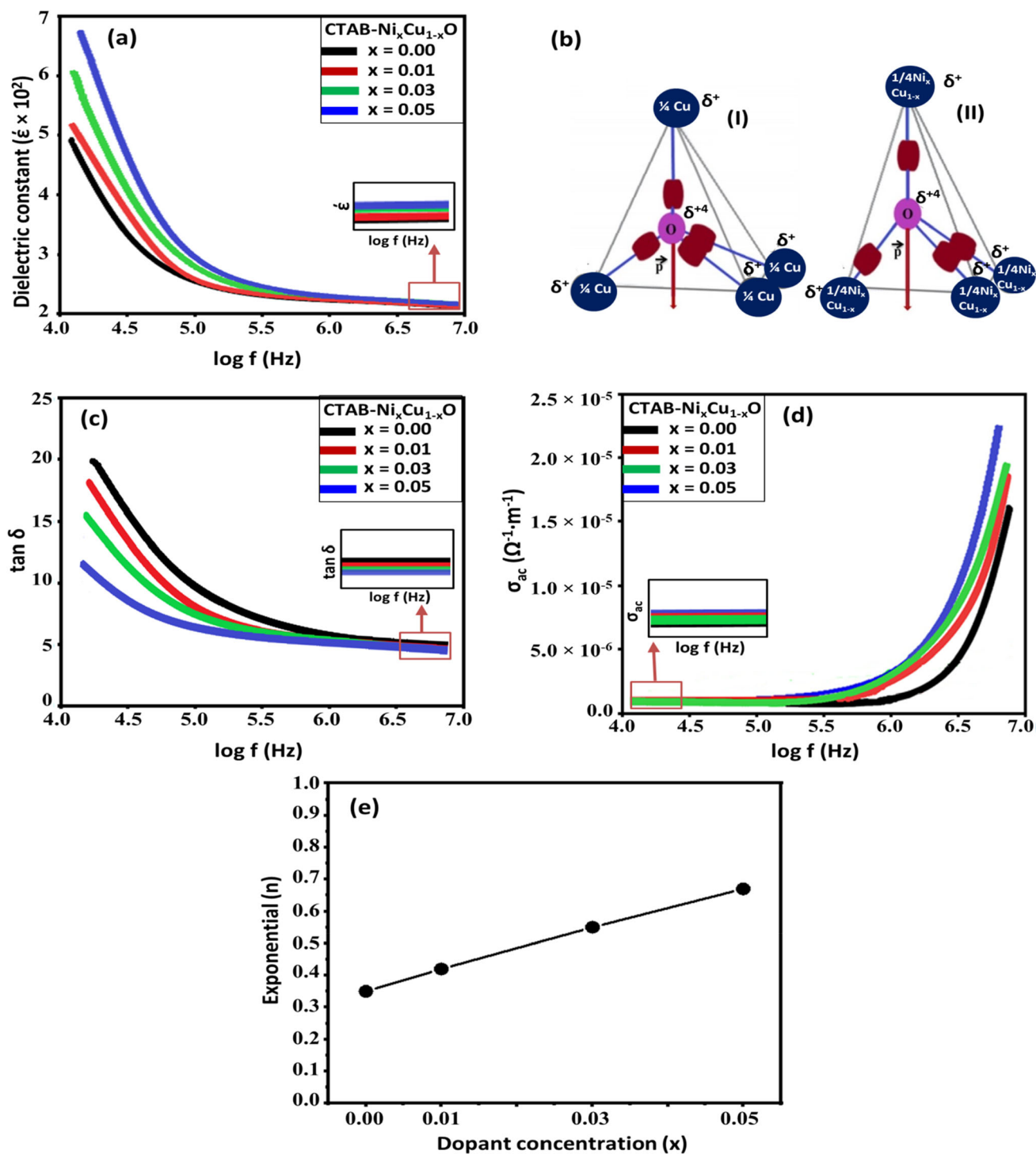


**Figure 7** Real part of the relative permittivity (a) Co-ordinated oxygen atom by four copper atoms (b-I), Co-ordinated oxygen atom by four CTAB-Ni<sub>x</sub>Cu<sub>1-x</sub>O of high electronegativity (b-II)

Dielectric tangent loss (c) AC electrical conductivity (d) and variation of frequency exponent ( $n$ ) with dopant concentration (e) for all prepared samples.

boundaries. The charge carrier accumulation leads to large polarization (Interface polarization) at grain boundaries, demonstrating a high dielectric constant

at lower frequencies. Further, the interface polarization is gradually reducing with increasing frequency because the hopping process can no longer follow the

applied field frequency, resulting in a low dielectric constant [68]. As a result, the high dielectric constant at the low-frequency region drops to a lower value and then attains approximately a constant value in higher and higher frequencies. It is also evident from the inset of Fig. 7a that the Ni doping gradually increases the  $\epsilon$  value of CuO, which may originate from the enhanced Pauling electronegativity of Ni (1.9) than that of the Cu (1.8) atom. In the CuO compound, each Cu atom is co-ordinated with four O atoms, where the strengthened electron density exists at the O atom in the form of a distorted tetrahedron as illustrated in Fig. 7b-I and II. The wider bond angle due to the presence of electron density nearly central O atom is resulting in small polarizability of the materials. The electronegativity of the system increases with the addition of Ni ions, causing the electron density shift toward Cu ( $\text{Ni}_x\text{Cu}_{1-x}$ ) atoms, which consequently decreases the bond angle leading to enhanced polarization effect through resulting high value of dielectric constant at high doping concentration ( $x$ ) as shown in Fig. 7b-II. This assignment is consistent with the previously published work of the literature [69, 70]. The contributing species to polarizability is lagging behind the applied AC field estimates energy dissipation in a dielectric system and is denoted by dielectric loss tangent. Figure 7c illustrates the dielectric loss tangent ( $\tan\delta$ ) of the synthesized samples as a function of frequency and dopant concentration ( $x$ ). It is found that the high value of  $\tan\delta$  at the lower frequency region starts decreasing by increasing  $\log(f)$  and eventually attains almost a constant value for all the samples. The high  $\tan\delta$  at lower frequency region or low  $\tan\delta$  at higher frequencies and the non-existence of any loss peak defines a charge carrier-controlled system, where the dominant contribution arises from the synergy of the metallic nature of Ni-dopant and cationic CTAB capping of CuO. The decreasing trend of the  $\tan\delta$  as a function of  $\log(f)$  is attributed to the dipoles lag behind to the applied AC field. The lowering of  $\tan\delta$  was observed both in low- and high-frequency regions by increasing Ni doping concentration ( $x$ ), which might be due to the grain boundary resistance [71]. The AC conductivity ( $\sigma_{ac}$ ) for all samples increases slowly in low-frequency but sharply in higher frequency regions, as shown in Fig. 7d. This phenomenon has commonly been observed in many cases [31, 71–73]. The frequency-dependent AC

conductivity of the prepared NPs at room temperature can be explained using the power's law.

$$\sigma_{ac} \propto \log(f)^n \quad (6)$$

where  $\sigma_{ac}$  denotes the AC electrical conductivity,  $f$  is the applied electric field frequency, and exponential  $n$  denotes the slop (increase in the AC conductivity) depends on applied field frequency. By taking Eq. (6) into account, the AC conductivity of the products strictly depends on the variation of the exponential ( $n$ ) with the applied field frequency ( $f$ ) and dopant concentrations ( $x$ ). The exponential ( $n$ ) is calculated from the linear fitting of  $\sigma_{ac}$  and  $\log f$  curves at varying doping concentration as depicted in Fig. 7e. It is shown that the value of exponential ( $n$ ) increases ( $0 \leq n \leq 1$ ) with the increase of Ni doping ( $0 \leq x \leq 0.05$ ), indicating the hopping conduction of charge carriers. Thus, the increase in AC conductivity is attributed to the hopping model, where a strengthened hopping of charge carrier phenomenon takes place at higher frequencies [71, 74, 75]. The AC conductivity is also enhanced like a real part of dielectric constant with Ni doping concentrations ( $x$ ), which might be due to the increasing hopping frequency effect [71]. Thus, the improved dielectric behavior ( $\epsilon$  and  $\tan\delta$ ) and AC conductivity ( $\sigma_{ac}$ ) as a function of frequency and Ni doping concentrations ( $x$ ) promote the practical use of the CTAB- $\text{Ni}_x\text{Cu}_{1-x}\text{O}$  NPs as interconnected nanoagent for high quality of the healthcare purposes. This is because, the electrostatic interaction between positively charged NPs and negatively charged cellular surfaces causes microbial cell growth inhibition, determining an important antimicrobial aspect in the healthcare sector [76].

The improved optical and dielectric properties of the developed CTAB-capped  $\text{Ni}_x\text{Cu}_{1-x}\text{O}$  ( $0.0 \leq x \leq 0.05$ ) NPs can make the resulting materials amenable for in vitro antibacterial activity applications. In this regard, the effect of the well-grown NPs on the two different Gram + Ve (*C. albicans* (24433-ATCC), *S. aureus* (25923-ATCC)) and two type of Gram –Ve (*E. coli* (25922-ATCC), *K. pneumoniae* (7000603)) pathogenic strains of bacteria are analyzed using Agar well diffusion method as shown in Fig. 8. It indicates that all samples have pronounced antimicrobial effects on pathogens and demonstrate distinctive inhibitory zone diameter with Ni loading. Table 2 provides the CLSI (clinical and laboratory standard institute) criteria that determine the

bactericidal susceptibility in terms of ZOI (zone of inhibition). Comparing the obtained data and results of ZOI (Table 3) with the CLSI criteria of the zone diameter values, it is obvious that the CTAB-capped Ni modified CuO NPs are effective isolates against *S. aureus*, *K. pneumoniae* and *E. coli* while showing moderate-level performance toward *C. albicans* growth inhibition. The intermediate activity is also acceptable for *C. albicans* growth suppression at maximum ( $60 \mu\text{g ml}^{-1}$ ) concentration when compared with the previously reported work of S. Talal et al. [77], which showed the least (8 mm) inhibitory zone for *C. albicans* at  $0.01 \text{ mg ml}^{-1}$  concentration. The combat performance of the developed nanomaterials is tested with different concentrations of  $0 \mu\text{g ml}^{-1}$ ,  $5 \mu\text{g ml}^{-1}$ ,  $15 \mu\text{g ml}^{-1}$ ,  $30 \mu\text{g ml}^{-1}$ ,  $45 \mu\text{g ml}^{-1}$  and  $60 \mu\text{g ml}^{-1}$  as illustrated in Table 3. In the absence of the CTAB- $\text{Ni}_x\text{Cu}_{1-x}\text{O}$  NPs treatment, the zone of inhibition was not observed and the growth of all four tested species reaches to exponential phase (Fig. 8a1–a4). However, when exposed to varying concentrations (5, 15, 30, 45, and  $60 \mu\text{g ml}^{-1}$ ) of CTAB- $\text{Ni}_x\text{Cu}_{1-x}\text{O}$  ( $0.0 \leq x \leq 0.05$ ) NPs suspension, inhibitory effect on the growth of pathogens with respect to the zone of inhibition is demonstrated as shown in Fig. 8b1–b4. When using the CTAB- $\text{Ni}_x\text{Cu}_{1-x}\text{O}$  ( $x = 0.05$ ) sample, the MIC study against *S.*

**Table 2** CLSI criteria for ZOI (zone of inhibition)

Antibacterial agent	Inhibitory zone diameter (mm)		
	Susceptible	Intermediate	Resistant
CTAB- $\text{Ni}_x\text{Cu}_{1-x}\text{O}$	> 20	15–19	< 14

*aureus* and *K. pneumoniae* bacteria is extremely low as compared to *E. coli* and *C. albicans* bacteria. Motamedifar et al. [78] reported the MIC (10, 25, and  $50 \mu\text{g ml}^{-1}$ ) study of CuO nanoparticles against different microbial strains with admirable antimicrobial activity, except inferior performance, was seen for  $10 \mu\text{g ml}^{-1}$  dose against *S. aureus*. In our case, even 15 and  $5 \mu\text{g ml}^{-1}$  doses of CTAB- $\text{Ni}_x\text{Cu}_{1-x}\text{O}$  for  $x = 0.03$  and 0.05 samples suppressed *S. aureus* stain with the maximum zone inhibition of  $31 \pm 0.6 \text{ mm}$  and  $32 \pm 0.3 \text{ mm}$ , respectively. Particularly, only a  $5 \mu\text{g ml}^{-1}$  dose of CTAB-capped  $\text{Ni}_x\text{Cu}_{1-x}\text{O}$  ( $x = 0.05$ ) sample presents excellent growth inhibition of *K. pneumoniae* strain with zone of inhibition  $31 \pm 0.2 \text{ mm}$ , which is one-tenth times higher than the result reported by Dwivedi and co-workers [41] in gum acacia-modified Ni-doped CuO nanostructures. Further, the maximum concentration ( $60 \mu\text{g ml}^{-1}$ ) of the CTAB- $\text{Ni}_x\text{Cu}_{1-x}\text{O}$  ( $x = 0.05$ ) sample

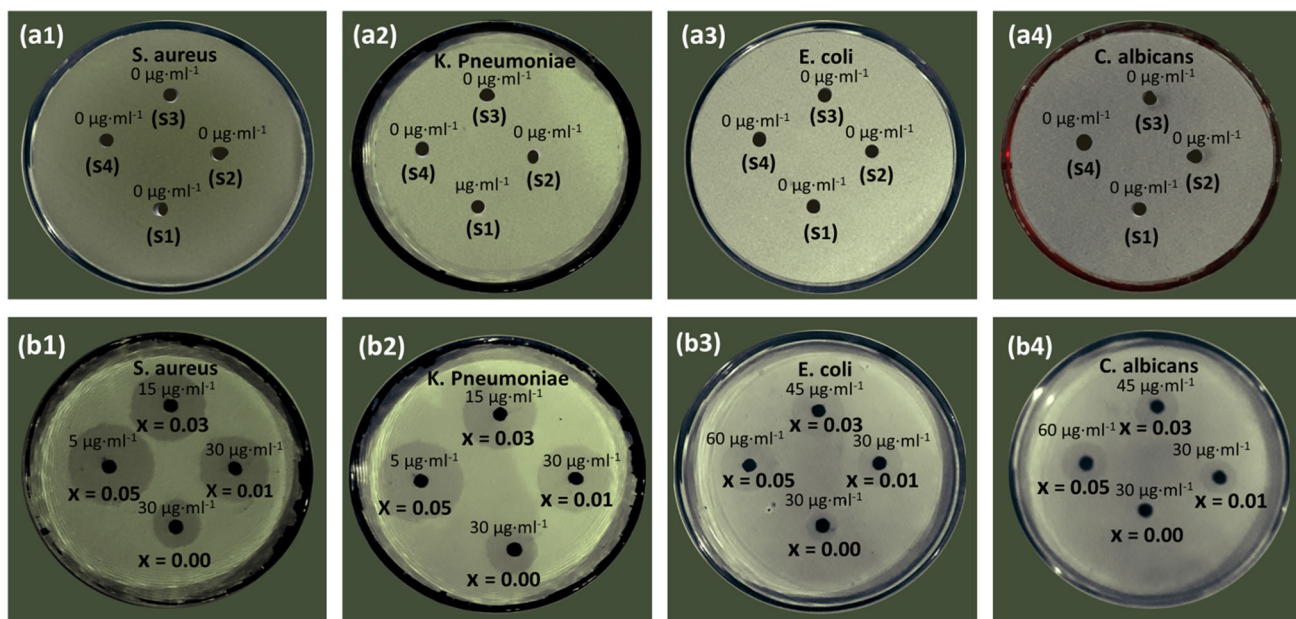


**Figure 8** Digital images of the zone of inhibition for *S. aureus*, *K. pneumoniae*, *E. coli*, and *C. albicans* at  $37^\circ\text{C}$  for 18 h. **a1–a4** control group at  $0 \mu\text{g ml}^{-1}$  and **b1–b4** CTAB- $\text{Ni}_x\text{Cu}_{1-x}\text{O}$

( $x = 0.00$ , 0.01, 0.03, and 0.05) samples with different concentrations ( $5$ ,  $15$ ,  $30$ ,  $45$ , and  $60 \mu\text{g ml}^{-1}$ ).

**Table 3** The MIC and mean diameter (mm) ZOI of the blank and CTAB-Ni<sub>x</sub>Cu<sub>1-x</sub>O samples against Gram Positive/Negative strains

Concentrations (μg ml <sup>-1</sup> )	Inhibition zone (mm) ± SD <i>S. aureus</i> (ATCC 25923)	Sensitive	Concentrations (μg ml <sup>-1</sup> )	Inhibition zone (mm) ± SD <i>C. albicans</i> (ATCC 24433)	Sensitive
<i>Gram positive bacteria</i>					
Blank sample	0.00 ± 0.00	Nil	Blank sample	0.00 ± 0.00	Nil
CTAB-CuO—30	23.3 ± 0.7	Susceptible	CTAB-CuO—30	0.00 ± 0.00	Nil
CTAB-Ni <sub>0.01</sub> Cu <sub>0.99</sub> O—30	27.2 ± 0.9	Susceptible	CTAB-Ni <sub>0.01</sub> Cu <sub>0.99</sub> O—30	10.7 ± 0.6	Resistant
CTAB-Ni <sub>0.03</sub> Cu <sub>0.97</sub> O—15	31.0 ± 0.6	Susceptible	CTAB-Ni <sub>0.03</sub> Cu <sub>0.97</sub> O—45	14.3 ± 0.8	Intermediate
CTAB-Ni <sub>0.05</sub> Cu <sub>0.95</sub> O—05	32.0 ± 0.3	Susceptible	CTAB-Ni <sub>0.05</sub> Cu <sub>0.95</sub> O—60	17.0 ± 0.5	Intermediate
Concentrations (μg ml <sup>-1</sup> )	Inhibition zone (mm) ± SD <i>K. pneumonia</i> (ATCC 700603)	Sensitive	Concentrations(μg ml <sup>-1</sup> )	Inhibition zone (mm) ± SD <i>E. coli</i> (ATCC 25922)	Sensitive
<i>Gram negative bacteria</i>					
Blank sample	0.00 ± 0.00	Nil	Blank sample	0.00 ± 0.00	Nil
CTAB-CuO—30	21.4 ± 0.5	Susceptible	CTAB-CuO—30	10.5 ± 0.8	Resistant
CTAB-Ni <sub>0.01</sub> Cu <sub>0.99</sub> O—30	25.0 ± 0.9	Susceptible	CTAB-Ni <sub>0.01</sub> Cu <sub>0.99</sub> O—30	15.7 ± 0.9	Intermediate
CTAB-Ni <sub>0.03</sub> Cu <sub>0.97</sub> O—15	29.0 ± 0.3	Susceptible	CTAB-Ni <sub>0.03</sub> Cu <sub>0.97</sub> O—45	21.2 ± 0.5	Susceptible
CTAB-Ni <sub>0.05</sub> Cu <sub>0.95</sub> O—05	31.0 ± 0.2	Susceptible	CTAB-Ni <sub>0.05</sub> Cu <sub>0.95</sub> O—60	21.4 ± 0.3	Susceptible

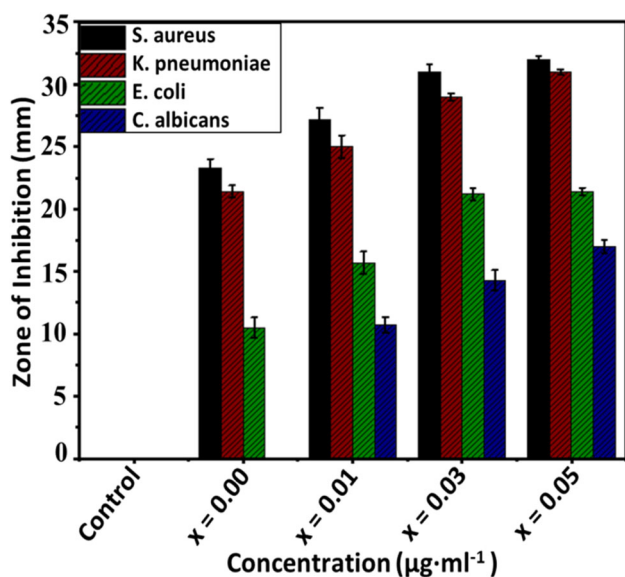
suppressed the *E. coli* growth with the area of zone of inhibition  $21.4 \pm 0.3$  mm and less effective against *C. albicans* where the zone of inhibition is  $17 \pm 0.5$  mm as depicted in Fig. 8b3 and b4, respectively. The lowest zone of inhibition for *C. albicans* compared to the rest of the pathogens indicates that CuO NPs up-to  $60 \mu\text{g ml}^{-1}$  concentration has no significant effect on the *C. albicans* growth suppression. In the previous report of M. Amri et al. [79] revealed the similar investigation as in this experimental work where the lower concentrations ( $1\text{--}100 \mu\text{g ml}^{-1}$ ) of CuO nanoparticles almost inhibited 30–40% growth of *C. albicans*. A. Karimiyan et al. [80] reported similar study of CuO nanoparticles against *C. albicans* where they revealed that the  $400 \mu\text{g ml}^{-1}$  dose can inhibit the growth of *C. albicans* with larger zone of inhibition. The less antifungal activity of our products against *C. albicans* is still satisfactory at  $60 \mu\text{g ml}^{-1}$  minimum dose compared to the previous reported works and the control counterpart and the effect can be increased at higher concentrations. However, the size and shape of the nanomaterials can affect the antimicrobial performance and lead to different biological results in these types of experiments [81]. It is worth mentioning that, there are different works available on the antimicrobial activities of the CuO nanostructures against various bacterial strains prepared by different synthetic routes, as presented in Table 4. These nanomaterials certainly play an essential role in high antimicrobial efficacy to both

type of Gram + Ve and Gram -Ve pathogenic bacterial strains due to their preferred shape, size, and chemical stability. In this respect, we synthesized our engineered materials using a solvothermal method with unique sizes and spherical morphologies, demonstrating high eradicating activity to *S. aureus* (+ ve), *K. pneumonia* (-ve), and *E. coli* (-ve) as well as exhibit moderate performance against *C. albicans* (+ ve) at different concentrations (5, 15, 30, 45, and  $60 \mu\text{g ml}^{-1}$ ). A close inspection declared that CTAB-Ni<sub>0.05</sub>Cu<sub>0.95</sub>O NPs demonstrate excellent bactericidal performance compared to the rest of the samples as shown in Fig. 9.

It can be concluded from the above discussion that the CTAB-capped undoped and Ni-doped CuO NPs demonstrate significant antibacterial resistance to two different type of Gram + Ve and Gram -Ve species. However, the exact mechanism of bacterial growth suppression while using chemically modified CuO is of great importance but not yet fully understood [82]. So far the exact mechanism, several interpretations are available that determine nanomaterials toxicity against different MDRs microbes [83–85]. The first and most simple mechanism is the direct reaction of CuO NPs with the bacterial membrane, disrupting the cell-wall and eventually killing the microorganism. In this case, the particle size and morphology play a vital role as a nanoagent’s bactericidal effect [86]. The second straight forward mechanism is the release of  $\text{Cu}^+/\text{Cu}^{+2}$  ions in the

**Table 4** The relative antibacterial study of prepared nanomaterials with literature

	Synthesis techniques	Nanomaterials	Dose of nanomaterials	Antibacterial Results	
Literature reported works	Gel-combustion technique [11]	CuO	Frequently used more than $5 \mu\text{g ml}^{-1}$ concentration	<i>S. aureus</i> is more susceptible	
	Hydrothermal technique [28]	Mg and Ce modified CuO			
	Sonochemical method [27]	Zn incorporated CuO			
	Microwave-assisted technique [38]	Ag/Co co-doped CuO			
	Mixed wet chemical technique [22]	Ag/CuO			
	Sol–Gel technique [95]	Zn/CuO			<i>E. coli</i> is more susceptible
	Chemical precipitation technique [26]	Ni/CuO			
	Sol–Gel Process [25]	Fe/CuO			
	Sol–Gel method [96]	Cu, CuO			
	Sonochemical method [97]	PANI-CuO			<i>K. pneumoniae</i> is more susceptible
This work	Solvothermal method	CTAB- $\text{Ni}_x\text{Cu}_{1-x}\text{O}$	$5 \mu\text{g ml}^{-1}$	<i>S. aureus</i> and <i>K. pneumoniae</i> are more susceptible than <i>E. coli</i> and <i>C. albicans</i>	

**Figure 9** Antimicrobial activity of the control group at  $0 \mu\text{g}\cdot\text{ml}^{-1}$  and CTAB- $\text{Ni}_x\text{Cu}_{1-x}\text{O}$  ( $x = 0.00, 0.01, 0.03$  and  $0.05$ ) samples at different concentrations ( $5, 15, 30, 45,$  and  $60 \mu\text{g ml}^{-1}$ ).

culture medium that generates oxidative stress, then cross the bacterial cell wall, and finally disrupts the

bacterial cell membranes' enzyme. The third and most crucial antibacterial mechanism is the excess amount of ROS generation in the bacterial culture medium. These ROS include singlet oxygen ( $\text{O}_2$ ), superoxide radical  $\text{O}_2^-$ , and hydrogen peroxide ( $\text{H}_2\text{O}_2$ ), which induces oxidative stress on the cell membrane. The ultra-small particle size, spherical morphology, and increased amount of active sites provide a better chance to cross the bacterial membrane and inhibit the bacterial growth so as to die the microorganism, which conquers the predominant antibacterial mechanism of NPs [87, 88]. On the other hand, the dissolution of CuO NPs and the successive detachment of  $\text{Cu}^+/\text{Cu}^{2+}$  ions during a cycle (Haber–Weiss–Fenton) further increase the ROS production rate. The direct penetration of  $\text{H}_2\text{O}_2$  (hydrogen peroxide),  $\text{OH}^\bullet$  (hydroxyl), and  $^1\text{O}_2$  (singlet oxygen) radicals of ROS into the bacterial cells disrupt membrane structure integrity, malfunction, cell proteins, lipids, and DNA of the cell wall, operating to the inhibition of bacterial growth and death [89–92]. It is worth mentioning that all aerobic organisms produce



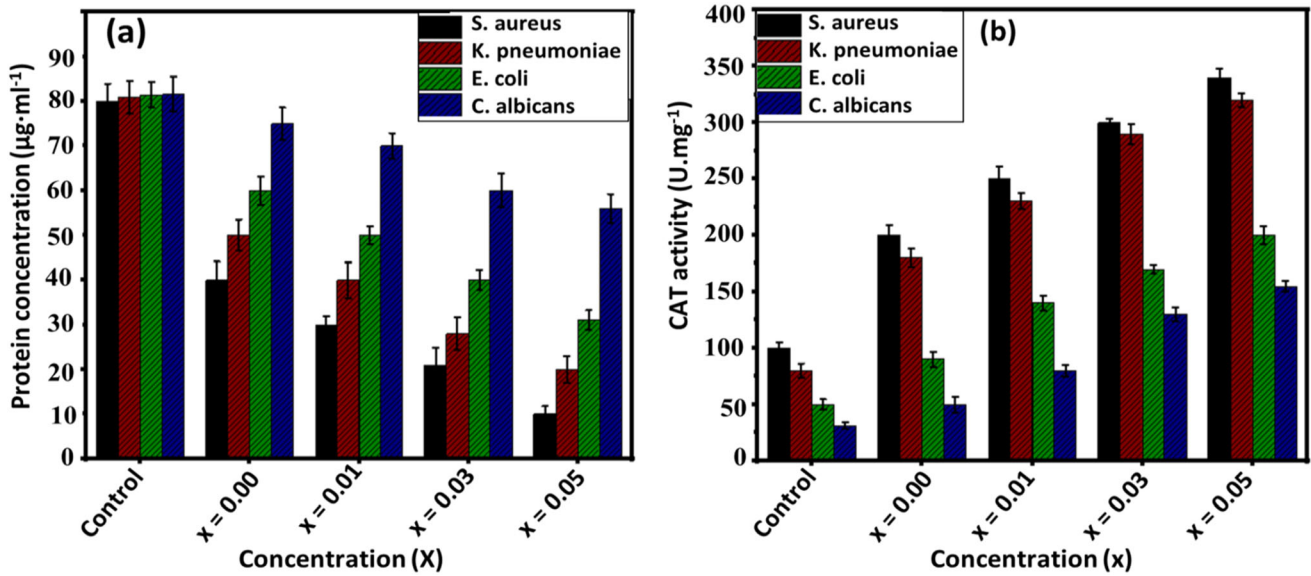
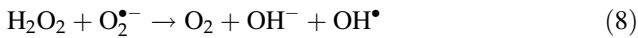
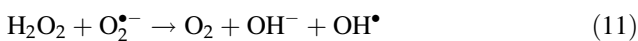
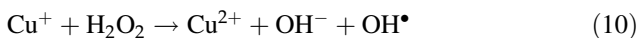


Figure 10 Protein concentrations (a) and CAT activity (b) in the tested microbes, respectively.

ROS as a byproduct of bacterial cellular respiration, as given [93].



During normal situation, the bacterial cells produce endogenous substances (free radical scavengers) that produce a chemical reaction with free-radicals and yield stable molecules. These stable molecules prevent the damage of mitochondrial respiratory chain reaction [94]. However, when Cu<sup>+</sup>/Cu<sup>2+</sup> ions enter the culture medium, the chain reaction results in damage to the cell membrane and DNA and disrupt the enzyme system of bacteria [89]. This effect arises due to the increase in the ROS generation rate as follows [92].



It is noteworthy that the mechanism of the bacterial cell damage caused by free radicals and free radicals scavengers plays a central role in a cell injury so as to cell death. In contrast to ROS scavengers, the increased concentration of OH<sup>•</sup> radicals creates highly oxidative damage to bacterial cell membranes, inhibiting the bacterial growth and eventually killing the bacteria [91]. To further divulge the antibacterial activity of the prepared samples, the protein level

and catalase activity in all four tested microbes are designed and presented in Fig. 10a and b respectively. The protein level in all four bacterial strains decreases in contrast to the control group, confirms that both pure and doped CTAB-CuO significantly inactivated proteins in the bacterial cells. Compared to the control group, all four microbes' catalase activity shows an increasing trend with doping concentrations (x), indicating the increase of H<sub>2</sub>O<sub>2</sub> level in the cell membranes. These results prove strong intracellular ROS generation in the doped CTAB-CuO samples.

To sum up the above discussion and the results obtained in this study, it can be concluded that the antimicrobial activity of the CTAB-capped Ni<sub>x</sub>-Cu<sub>1-x</sub>O NPs is intensively dependent on the release of Cu<sup>+</sup>/Cu<sup>2+</sup> ions and ROS production rate. The detached Cu<sup>+</sup>/Cu<sup>2+</sup> ions further produce a chemical reaction with functional groups such as -OH (hydroxyl-group), -SH (sulfhydryl-group) group, and -NH<sub>2</sub> (amino-group) to damage the protein chain in bacteria, which is consistent with the decreased in protein level in all four tested pathogens. On the contrary, antimicrobial cationic surfactant (CTAB) and Ni-dopant-treated CuO leads to the lattice defects, lattice strains, and an excess amount of active sites collectively induce enhanced ROS generations, which produce oxidative stress until the balance gets damage. Thus, the factors that are boosting the antimicrobial properties of CTAB-capped Ni<sub>x</sub>Cu<sub>1-x</sub>O

NPs may be attributed to the direct penetration of NPs into the cell membrane, release of  $\text{Cu}^+/\text{Cu}^{2+}$  ions in the culture medium, excess amount of ROS generation as well as the synthesis method to achieve materials with the desired size and surface morphology. It is also quite possible that materials with the tuned band gap and high dielectric permittivity execute high antibacterial susceptibility to broad range of microorganisms for the effective treatment of various microbial infections.

## Conclusions

In summary, the CTAB-capped  $\text{Ni}_x\text{Cu}_{1-x}\text{O}$  NPs with varying doping concentrations ( $0.00 \leq x \leq 0.05$ ) were synthesized using a facile one-step solvothermal method to investigate the doping-induced effect on optical, dielectric, and antibacterial properties of CuO. The physical quantitative analysis using XRD, SEM, TEM, and EDS confirm the successful substitution of Ni into the CuO matrix with a reduction in the grain size, the cationic surfactant (CTAB) effectively serves as a capping agent, and the presence of expected elemental composition in the compounds, respectively. The FT-IR spectra further confirm the phase purity by Cu–O bond formation and CTAB coating on CuO. Enhanced optical band gap is observed for highly doped CuO samples, revealing a blue shift with Ni doping concentrations ( $x$ ). The dielectric behavior (real part of dielectric constant and tangent loss) and AC conductivity of the samples show frequency and dopant-dependent nature, calculated from the power's law. The improved dielectric performance (with high AC conductivity) and tailored band gap energy ( $E_g$ ) make these nanomaterials innovative for antimicrobial activity applications. According to the antimicrobial results of the synthesized products, the CTAB- $\text{Ni}_{0.05}\text{Cu}_{0.95}\text{O}$  sample exhibits maximum growth inhibition against MDRs pathogenic *S. aureus* and *K. pneumoniae* content for extremely low MIC value of  $5 \mu\text{g ml}^{-1}$ , respectively. The enhanced dose-dependent antimicrobial performance is mainly originated from the several important factors of physical variation in the band gap energy ( $E_g$ ), dielectric behavior ( $\epsilon$  and  $\tan\delta$ ), and AC conductivity ( $\sigma_{ac}$ ), as well as the synthesis method to achieve materials with the unique size and surface morphology. The contribution of Ni-dopant and cationic surfactant CTAB collectively leads to

structural defects and creates an excess of positive charge on the surface of CuO, leading to more ROS generation and produce highly oxidative stress on bacterial cells. These findings suggest that the correlative doping and coating is a promising strategy for enhancing the antimicrobial efficiency of nanomaterials for the required applications.

## Acknowledgements

The authors (B. Yuan, Y. Yan, and B.A. Shah) are thankful for the grants from the Training Program of Major Basic Research Project of Provincial Natural Science of Guangdong (2017B030308001). The authors are also very grateful to the International Islamic University Islamabad (IIU), Pakistan, for research facilities.

## Declarations

**Conflict of interest** The authors declare no competing financial interest.

## References

- [1.] Farjadian F, Ghasemi A, Gohari O, Roointan A, Karimi M (2019) Nanopharmaceuticals and nanomedicine currently on the market: challenges and opportunities. *Nanomedicine* (London) 14(1):93–126. <https://doi.org/10.2217/nmm-2018-0120>
- [2.] Tanwar J, Das S, Fatima Z, Hameed S (2014) Multidrug resistance: an emerging crises. *Interdiscip Perspect Infect Dis* 2014:541340. <https://doi.org/10.1155/2014/541340>
- [3.] Munoz-Escobar A, Reyes-López SY (2020) Antifungal susceptibility of *Candida* species to copper oxide nanoparticles on polycaprolactone fibers (PCL-CuONPs). *PLoS ONE* 15(2):e0228864. <https://doi.org/10.1371/journal.pone.0228864>
- [4.] Spellberg B, Blaser M, Guidos R, Boucher H, Bradley J, Eisenstein BI (2011) Combating antimicrobial resistance: policy recommendations to save lives. *Clin Infect Dis* 52:S397–S428. <https://doi.org/10.1093/cid/cir153>
- [5.] Basak S, Singh P, Rajurkar M (2016) Multidrug-resistant and extensively drug-resistant bacteria: a study. *J Pathog* 2016:1–5. <https://doi.org/10.1155/2016/4065603>
- [6.] Costerton JW, Stewart PS, Greenberg EP (2016) Bacterial biofilms: a common cause of persistent infections. *Science* 284:1318–1322. <https://doi.org/10.1126/science.284.5418.1318>

- [7.] Kim MH (2016) Nanoparticle-based therapies for wound biofilm infection: opportunities and challenges. *IEEE Trans Nanobiosci* 15(3):294–304. <https://doi.org/10.1109/TNB.2016.2527600>
- [8.] Flemming HC, Wingender J, Szewzyk U (2016) Biofilms: an emergent form of bacterial life. *Nat Rev Microbiol* 14(9):563–575. <https://doi.org/10.1038/nrmicro.2016.94>
- [9.] Hu X, Kang F, Yang B, Zhang W (2019) Extracellular polymeric substances acting as a permeable barrier hinder the lateral transfer of antibiotic resistance. *Front Microbiol* 10:736. <https://doi.org/10.3389/fmicb.2019.00736>
- [10.] Bjarnsholt T, Ciofu O, Molin S, Givskov M (2013) Applying insights from biofilm biology to drug development. *Nat Rev Drug Discov* 12(10):791–808. <https://doi.org/10.1038/nrd4000>
- [11.] Aggarwall T, Wadhwa R, N, Thaoliyal, (2019) Recent trends of nanomaterials as antimicrobial agents. *Nanotechnol Mod Anim Biotechnol* 13:978–981. [https://doi.org/10.1007/978-981-13-6004-6\\_5](https://doi.org/10.1007/978-981-13-6004-6_5)
- [12.] Yaqoob AA, Ahmad A, Parveen T, Ahmad A, Oves M (2020) Recent advances in metal decorated nanomaterials and their various biological applications: a review. *Front Chem* 8:341. <https://doi.org/10.3389/fchem.2020.00341>
- [13.] Azam A, Ahmad A, Oves M, Khan M, Habib S, Memic A (2012) Antimicrobial activity of metal oxide nanoparticles against Gram-positive and Gram-negative bacteria: a comprehensive study. *Int J Nanomed* 7:6003–6009. <https://doi.org/10.2147/IJN.S35347>
- [14.] Khairnar SD, Shinde S, Shrivastava VS (2019) A short review on the improvement of antimicrobial activity by metal and nonmetal doping in nanoscale antimicrobial materials. *Nanomed Biother Discov* 9(1):163. <https://doi.org/10.4172/2155-983X.1000163>
- [15.] Bhattacharya P, Neogi S (2018) Antibacterial properties of doped nanoparticles. *Rev Chem Eng* 35(7):861–876. <https://doi.org/10.1515/revce-2017-0116>
- [16.] Ranghar S, Sirohi P, Verma P, Agarwal V (2014) Nanoparticle-based drug delivery systems: promising approaches against infections. *Braz Arch Biol Technol* 57(2):209–222. <https://doi.org/10.1590/S1516-89132013005000011>
- [17.] Covarrubias P (2013) Nanoparticles in drug delivery: past, present and future. *Adv Drug Deliv Rev* 65(1):21–23. <https://doi.org/10.1016/j.addr.2012.04.010>
- [18.] Wang Z, Hu T, Liang R, Wei M (2020) Application of zero-dimensional nanomaterials in biosensing. *Front Chem* 8:320. <https://doi.org/10.3389/fchem.2020.00320>
- [19.] Chang YN, Zhang M, Xia L (2012) The toxic effects and mechanisms of CuO and ZnO nanoparticles. *Materials* 5(12):2850–2871. <https://doi.org/10.3390/ma5122850>
- [20.] Ojas M, Bhagat M, Gopalakrishnan C (2008) Ultrafine dispersed CuO nanoparticles and their antibacterial activity. *Exp Nanosci* 3(3):185–193. <https://doi.org/10.1080/17458080802395460>
- [21.] Mantecca P, Moschini E, Bonfanti P, Fascio U, Kedenken A (2015) Toxicity evaluation of a new Zn-doped CuO nanocomposites with highly antibacterial properties. *Toxicol Sci* 146(1):16–30. <https://doi.org/10.1093/toxsci/kfv067>
- [22.] Asamoah RB, Annan E, Mensah B, Nbelayim P, Apalangya V, Onwona-Agyeman B, Yaya A (2020) A comparative study of antibacterial activity of CuO/Ag and ZnO/Ag Nanocomposites. *Adv Mater Sci Eng* 2020:7814324. <https://doi.org/10.1155/2020/7814324>
- [23.] Duffy LL, Osmond-McLeod MJ, Judy J, King T (2018) Investigation into the antibacterial activity of silver, zinc oxide and copper oxide nanoparticles against poultry-relevant isolates of *Salmonella* and *Campylobacter*. *Food Control* 92:293–300. <https://doi.org/10.1016/j.foodcont.2018.05.008>
- [24.] Shkodenko L, Kassirov I, Koshel E (2020) Metal oxide nanoparticles against bacterial biofilms: perspectives and limitations. *Microorganisms* 8(10):1545. <https://doi.org/10.3390/microorganisms8101545>
- [25.] Pugazhendhi A, Kumar SS, Mayilmurugan M, Muthupandian S (2018) Photocatalytic and antimicrobial efficacy of Fe doped CuO nanoparticles against the pathogenic bacteria and fungi. *J Microb Pathog* 122:84–89. <https://doi.org/10.1016/j.micpath.2018.06.016>
- [26.] Yang J, Yin W, Zhou B, Cui A, Xu L, Zhang D, Li W, Hu Z, Chu J (2019) Composition dependence of optical properties and band structures in p-type Ni-doped CuO films: spectroscopic experiment and first-principles calculation. *J Phys Chem C* 123(44):27164–27171. <https://doi.org/10.1021/acs.jpcc.9b08604>
- [27.] Malka E, Perelshtein I, Lipovsky A, Shalom Y, Naparstek L, Perkas N, Patick T, Lubart R (2013) Eradication of multi-drug resistant bacteria by a novel Zn-doped CuO nanocomposites. *Small* 9(23):4069–4076. <https://doi.org/10.1002/sml.201301081>
- [28.] Lv Y, Li L, Yin P, Lei T (2020) Synthesis and evaluation of the structural and antibacterial properties of doped copper oxide. *Dalton Trans* 49:4699–4709. <https://doi.org/10.1039/D0DT00201A>
- [29.] Varghese D, Catherine T, Chandar NK (2017) Effect of CTAB on structural and optical properties of CuO nanoparticles prepared by co-precipitation route. *Mater Sci Eng* 263:022002. <https://doi.org/10.1088/1757-899X/263/2/022002>
- [30.] Amri SA, Ansari MS, Rafique S, Aldahri M, Rahimuddin S (2015) Ni-doped CuO nanoparticles: structural and optical

- characterizations. *Curr Nanosci* 11(2):191–197. <https://doi.org/10.2174/1573413710666141024212856>
- [31.] Baturay S, Tombak A, Kaya DK, Ocak YS, Tokus M (2016) Modification of electrical and optical properties of CuO thin films by Ni doping. *Sol–Gel Sci Technol* 78(2):422–429. <https://doi.org/10.1007/s10971-015-3953-4>
- [32.] Basith M, Vijaya J, Kennedy LJ, Bououdina M (2014) Structural, morphological, optical and magnetic properties of Ni-doped CuO nanostructures. *Mater Sci Semicond Process* 17:110–118. <https://doi.org/10.1016/j.mssp.2013.09.013>
- [33.] Sasikala R, Rani SK, Karthikeyan K, Easwaramoorthy D (2016) Synthesis and antibacterial studies of Lanthanum, Cerium and Ebrum loaded copper oxide nanoparticles. *Eng Chem Fuel* 1(4):43–51. <https://doi.org/10.18831/djchem.org/2016041004>
- [34.] Ramya S, Viruthagiri G, Gobi R, Shanmugam N, Kannadasan N (2016) Synthesis and characterization of Ni<sup>2+</sup> ions incorporated CuO nanoparticles and its application in antibacterial activity. *Mater Sci Mater Electron* 27(3):2701–2711. <https://doi.org/10.1007/s10854-015-4080-2>
- [35.] Nesa M, Momin MA, Sharmin M, Bhuiyan AH (2020) Structural, optical and electronic properties of CuO and Zn doped CuO: DFT based first-principles calculations. *Chem Phys* 528:110536. <https://doi.org/10.1016/j.chemphys.2019.110536>
- [36.] Kamble SP, Mote VD (2019) Structural, optical and magnetic properties of Co doped nanoparticles. *Solid State Sci* 95:105936. <https://doi.org/10.1016/j.solidstatesciences.2019.105936>
- [37.] Pugazhendhi A, Kumar SS, Manikandan M, Saravanan M (2018) Photocatalytic properties and antimicrobial efficacy of Fe doped CuO nanoparticles against the pathogenic bacteria and fungi. *Microb Pathog* 122:84–89. <https://doi.org/10.1016/j.micpath.2018.06.016>
- [38.] Thakur N, Anu K, Kumar (2020) Effect of (Ag, Co) co-doping on the structural and antibacterial efficiency of CuO nanoparticles. *J Environ Chem Eng* 8(4):104011. <https://doi.org/10.1016/j.jece.2020.104011>
- [39.] Magiorakos AP, Srinivasan A, Carey RB, Carmeli Y, Falagas ME, Giske CG (2012) Multidrug-resistant, extensively drug-resistant and pandrug-resistant bacteria: an international expert proposal for interim standard definitions for acquired resistance. *Clin Microb Infect* 18(3):268–281. <https://doi.org/10.1111/j.1469-0691.2011.03570>
- [40.] Thekkae Padil VV, Cernik M (2013) Green synthesis of copper oxide nanoparticles using gum karaya as a biotemplate and their antibacterial application. *Int J Nanomed* 8:889–898. <https://doi.org/10.2147/IJN.S40599>
- [41.] Dwivedi LM, Shukla N, Baranwal K, Gupta S, Siddiqui S, Singh V (2020) Gum acacia modified Ni doped CuO nanoparticles: an excellent antibacterial materials. *J Clust Sci* 32:209–219. <https://doi.org/10.1007/s10876-020-01779-7>
- [42.] Patterson AL (1939) The Scherrer formula for X-ray particle size determination. *Phys Rev* 56(10):978–982. <https://doi.org/10.1103/PhysRev.56.978>
- [43.] Cullity BD, Weymouth JW (1957) Elements of X-ray diffraction. *Am J Phys* 26(6):394–395. <https://doi.org/10.1119/1.1934486>
- [44.] Asbrink S, Norrby LJ (1970) A refinement of the crystal structure of copper(II) oxide with a discussion of some exceptiona. *Acta Crystallogr Sect B Struct Crystallogr Cryst Chem* 26(B):8–15. <https://doi.org/10.1107/S0567740870001838>
- [45.] Mrabet C, Boukhchem A, Amlouk M, Manoubi T (2016) Improvement of the optoelectronic properties of tin oxide transparent conductive thin film through lanthanum doping. *Alloys Compd* 666:392–405. <https://doi.org/10.1016/j.jallcom.2016.01.104>
- [46.] Mallika AN, Ramachandra AR, Sowri KB, Sujatha CH, Venugopal KR (2014) Structural and photoluminescence properties of Mg substituted ZnO nanoparticles. *Opt Mater* 36:879–884. <https://doi.org/10.1016/j.optmat.2013.12.015>
- [47.] Mehraj S, Ansari MS, Alimuddin A (2013) Structural, dielectric and complex impedance properties of Cd doped SnO<sub>2</sub> nanoparticles. *J Nanoeng Nanomanuf* 3(3):229–236. <https://doi.org/10.1166/jnan.2013.1137>
- [48.] Raghasudha M, Ravinder D, Veerasomaiah P (2013) Characterization of chromium substituted cobalt nano ferrites synthesized by citrate-gel auto combustion method. *Adv Mater Phys Chem* 3(2):89–96. <https://doi.org/10.4236/ampc.2013.32014>
- [49.] Eslami A, Modanlou N, Hosseini SG, Abbasi M (2017) Synthesis and characterization of CuO Nanoparticles by the chemical liquid deposition method and investigation of its catalytic effect on the thermal decomposition of ammonium perchlorate. *Cent Eur J Energ Mater* 14(1):152–168. <https://doi.org/10.22211/cejem/67560>
- [50.] Awad MA, Ahmed AM, Khavrus VO, Abraham EM (2015) Tuning the morphology of ZnO nanostructures by In doping and the associated variation in electrical and optical properties. *Ceram Int* 41(8):10116–10124. <https://doi.org/10.1016/j.ceramint.2015.04.108>
- [51.] Rios PR, Fonseca GS (2010) Grain boundary pinning by particles. *Mater Sci Forum* 638(642):3907–3912. <https://doi.org/10.4028/www.scientific.net/MSF.638-642.3907>
- [52.] Anli ST, Ebeoglugil MF, Celik E (2020) Effect of dopant elements on the structure and morphology of SnO<sub>2</sub>

- nanoparticles. *J Aust Ceram Soc* 56:403–411. <https://doi.org/10.1007/s41779-019-00344-4>
- [53.] Sui ZM, Chen X, Wang LY, Xu LM, Zhuang WC, Chai YC, Yang CJ (2006) Capping effect of CTAB on positively charged Ag nanoparticles. *Physica E* 33:308–314. <https://doi.org/10.1016/j.physe.2006.03.15>
- [54.] Kuzmenko AB, Van der Marel D, Van-Bentum PJ, Tishchenko EA, Presura C, Bush AA (2000) Extensive infrared spectroscopic study of CuO: signature of strong spin-phonon interaction and structural distortion. *Phys Rev B* 63(8):10060. <https://doi.org/10.1103/PhysRevB.63.094303>
- [55.] Thangamani C, Ponnar M, Priyadarshini P, Monisha P, Gomathi S (2019) Optical and magnetic behavior of Ni doped CuO. *Surf Rev Lett* 26(5):1793–6667. <https://doi.org/10.1142/S0218625X18501846>
- [56.] Debbichi L, Marco MC, Pierson JF, Kruger P (2012) Vibrational properties of CuO and Cu<sub>4</sub>O<sub>3</sub> from first-principles calculations, and Raman and Infrared spectroscopy. *Phys Chem C* 116(18):10232–10237. <https://doi.org/10.1021/jp303096m>
- [57.] Sarkar J, Chakraborty N, Chatterjee A, Bhattacharjee A, Dasgupta D, Acharya K (2020) Green synthesized copper oxide nanoparticles ameliorate defence and antioxidant enzymes in *Lens culinaris*. *Nanomaterials* (Basel) 10(2):312. <https://doi.org/10.3390/nano10020312>
- [58.] Tamil Selvi SS, Linet JM, Sagadevan S (2018) Influence of CTAB surfactant on structural and optical properties of CuS and CdS nanoparticles. *Exp Nanosci* 13(1):130–143. <https://doi.org/10.1080/17458080.2018.1445306>
- [59.] Zhang H, Liu Y, Zhu K, Xiong Y, Xiong C (1999) Infrared spectra of nanometer granular zirconia. *J Phys Condens Matter* 11(8):2035–2042. <https://doi.org/10.1088/0953-8984/11/8/016>
- [60.] Dahrul M, Alatas H, Irzaman (2016) Preparation and optical properties study of CuO thin film. *Procedia Environ Sci* 33:661–667. <https://doi.org/10.1016/j.proenv.2016.03.121>
- [61.] Borgohain K, Singh JB, Rao MR, Shripathi T, Mahamuni S (2000) Quantum size effects in CuO nanoparticles. *Phys Rev B* 61:11093–11096. <https://doi.org/10.1103/PhysRevB.61.11093>
- [62.] Moss TS, Burrell GJ, Ellis B (1973) Semiconductor optoelectronics. Butterworths, Heinemann, London, pp 1–474. <https://doi.org/10.1016/C2013-0-04197-7>
- [63.] Burstein E (1954) Anomalous optical absorption limit in InSb. *Phys Rev* 93:632–633. <https://doi.org/10.1103/PhysRev.93.632>
- [64.] Dhineshbabu NR, Rajendran V, Nithyavathy N (2016) Study of structural and optical properties of cupric oxide nanoparticles. *Appl Nanosci* 6:933–939. <https://doi.org/10.1007/s13204-015-0499-2>
- [65.] Singh DP, Srivastava ON (2009) Synthesis and optical properties of different CuO (Ellipsoid, Ribbon and Sheet Like) nanostructures. *Nanosci Nanotechnol* 9(9):5345–5350. <https://doi.org/10.1166/jnn.2009.1159>
- [66.] Tareev B, Troitsky A (1975) Physics of dielectric materials. Mir Publishers, Moscow
- [67.] Wagner KW (1973) The distribution of relaxation times in typical dielectrics. *Ann Phys* 40:817–819
- [68.] Koops CG (1951) On the dispersion of resistivity and dielectric constant of some semiconductors at audio frequencies. *Phys Rev* 83:121–124. <https://doi.org/10.1103/PhysRev.83.121>
- [69.] Melagiriyyappa E, Jayanna HS, Chougule BK (2008) Dielectric behavior and ac electrical conductivity study of Sm<sup>+3</sup> substituted Mg–Zn ferrites. *Mater Chem Phys* 112(1):68–73. <https://doi.org/10.1016/j.matchemphys.2008.05.014>
- [70.] Ahmad AS, Azam A (2012) Structural, Optical and Electrical properties of Ni doped CuO Nanoparticles. Department of applied Physics, Aligar Muslim University. Chapter 7:194–220. <http://hdl.handle.net/10603/11281>
- [71.] Norouzzadeh P, Mabhouti K, Golzan MM (2020) Comparative study on dielectric and structural properties of undoped, Mn-doped, and Ni-doped ZnO nanoparticles by impedance spectroscopy analysis. *J Mater Sci Mater Electron* 31:7335–7347. <https://doi.org/10.1007/s10854-019-02517-0>
- [72.] Sahay PP, Tewari S, Nath RK, Jha S, Shamsuddin M (2008) Studies on ac response of Zinc Oxide pellets. *Mater Sci* 43:4534–4540. <https://doi.org/10.1007/s10853-008-2641-x>
- [73.] Oruc C, Altindal A (2017) Structural and dielectric properties of CuO nanoparticles. *Ceram Int* 43(14):10708–10714. <https://doi.org/10.1016/J.CERAMINT.2017.05.006>
- [74.] Pollak M, Geballe TH (1961) Low-frequency conductivity due to hopping process in Silicon. *Phys Rev* 122:1742–1744. <https://doi.org/10.1103/PhysRev.122.1742>
- [75.] Elliot SR (1987) AC conduction in amorphous chalcogenide and pnictide semiconductors. *Adv Phys* 36:135–218. <https://doi.org/10.1080/00018738700101971>
- [76.] Sunilkumar M, Gafoor A, Anas A (2014) Dielectric properties: a gateway to antibacterial assay—a case study of low-density polyethylene/chitosan composite films. *J Polym* 46:422–429. <https://doi.org/10.1038/pj.2014.19>
- [77.] Abd ST, Ali AF (2015) Effect of zinc oxide nanoparticles on *Candida albicans* of human saliva (in vitro study). *Int J Res Dev Pharm Life Sci* 4(6):1892–1900. <https://doi.org/10.13187/ejm.2015.10.235>
- [78.] Sarai E, Heidari H, Razaee V, Mortazayi J, Motamedifar M (2018) Promising antibacterial effect of Copper Oxide

- nanoparticles against several multidrug resistant Uropathogens. *Pharm Sci* 24(3):213–218. <https://doi.org/10.15171/P.S.2018.31>
- [79.] Amiri M, Etemadifar Z, Daneshkazemi A, Nateghi M (2017) Antimicrobial Effect of copper oxide nanoparticles on some oral bacteria and candida species. *J Dent Biomater* 4(1):347–352
- [80.] Karimiyan A, Najafzadeh H, Ghorbanpour M, Hekmati-Moghaddam SH (2015) Antifungal effect of magnesium oxide, zinc oxide, silicon oxide and copper oxide nanoparticles against *Candida albicans*. *Zahedan J Res Med Sci*. 17(10):e2179. <https://doi.org/10.17795/zjrms-2179>
- [81.] Khan MF, Hameedullah M, Ansari AH, Ahmad E, Lohani MB, Khan RH, Alam MM, Khan W, Husain FM, Ahmad I (2014) Flower-shaped ZnO nanoparticles synthesized by a novel approach at near-room temperatures with antibacterial and antifungal properties. *Int J Nanomed* 9:853–864. <http://doi.org/10.2147/IJN.S47351>
- [82.] Bolla JM, Franco SA, Lik H, Evalier C, Mahmoud A, Boyer K (2011) Strategies for bypassing the membrane barrier in multidrug resistant Gram-negative bacteria. *FEBS Lett* 585(11):1682–1690. <https://doi.org/10.1016/j.febslet.2011.04.054>
- [83.] Thill A, Zeyon O, Spalla O, Chauvat F, Rose J, Auffan M, Flank AM (2006) Cytotoxicity of CeO<sub>2</sub> nanoparticles for *E. coli*: physico-chemical insight of cytotoxicity mechanism. *Environ Sci Technol* 40(19):6151–6156. <https://doi.org/10.1021/es060999b>
- [84.] Pardhi DM, Karaman DŞ, Timonen J, Wu W, Zhang Q, Satija S, Mehta M (2020) Antibacterial activity of inorganic nanomaterials and their antimicrobial peptide conjugates against resistant and non-resistant pathogens. *Int J Pharm* 586:0378–5173. <https://doi.org/10.1016/j.ijpharm.2020>
- [85.] Sawai J, Kawada E, Kanou F, Igarashi H, Hashimoto A, Kokugan T, Shimizu M (1996) Detection of active oxygen generated from ceramic powders having antibacterial activity. *J Chem Eng Jpn* 29(4):627–633. <https://doi.org/10.1252/jcej.29.627>
- [86.] Raghupathi KR, Koodali RT, Manna AC (2011) Size dependent bacterial growth inhibition and mechanism of antibacterial activity of ZnO nanoparticles. *Langmuir* 27(7):4020–4028. <https://doi.org/10.1021/la104825u>
- [87.] Ranghar S, Sirohi P, Verma P, Agarwal V (2012) Nanoparticles based drug delivery systems: promising approaches against infections. *Braz Arch Biol Technol* 57(2):209–222. <https://doi.org/10.1590/S1516-89132013005000011>
- [88.] Saleh NB, Milliron DJ, Aich N, Katz LE, Liljestrand HM (2016) Importance of doping, dopant distribution and defects on electronic band structure alteration of metal oxide nanoparticles: implication for reactive oxygen species. *Sci Total Environ* 568:926–932. <https://doi.org/10.1016/j.scitotenv.2016.06.145>
- [89.] Maurer-Jones MA, Gunsolus IL, Murphy CJ, Haynes CL (2013) Toxicity of engineered nanoparticles in the environment. *Anal Chem* 85(6):3036–3049. <https://doi.org/10.1021/ac303636s>
- [90.] Lin YE, Vidic RD, Stout JE, McCartney CA, Yu VL (2000) Inactivation of *Mycobacterium avium* by copper and silver ions. *Water Res* 32(7):1997
- [91.] Gajwicz A, Schaeublin N, Rasulev B, Hussain S, Puzyn T (2015) Towards understanding mechanisms governing cytotoxicity of metal oxides nanoparticles: hints from nano-QSAR studies. *Nanotoxicology* 9(3):313–325. <https://doi.org/10.3109/17435390.2014.930195>
- [92.] Stohs BSJ, Bagchi D (1995) Oxidative mechanisms in the toxicology of metal ions. *Free Radical Biol Med* 18(2):432–336. [https://doi.org/10.1016/0891-5849\(94\)00159-H](https://doi.org/10.1016/0891-5849(94)00159-H)
- [93.] Halliwell B, Gutteridge JMC (2015) Free radicals in biology and medicine. Oxford University Press, Oxford. <https://doi.org/10.1093/acprof:oso/9780198717478.001.0001>
- [94.] Ahmadinejad F, Moller SG, Bidkori G, Jami MS (2017) Molecular mechanisms behind free radical scavengers function against oxidative stress. *Antioxidants (Basel)* 6(3):51. <https://doi.org/10.3390/antiox6030051>
- [95.] Kumar P, Mathpal MC, Prakash J, Roos WD, Swart HC (2020) Bandgap tailoring of cauliflower-shaped CuO nanostructures by Zn doping for antibacterial applications. *Alloys Compd* 832:154958. <https://doi.org/10.1016/j.jallcom.2020.154968>
- [96.] Heli H, Golamhossein T, Sattarrahmady N, Rezvan DV, Hamed VK (2017) Nanoparticles of copper and copper oxides: synthesis and determination of antibacterial activity. *J Kerman Univ Med Sci* 24(2):166–170
- [97.] Thampi VVA, Rajan ST, Anupriya K (2015) Fabrication of fabrics with PANI/CuO nanoparticles by precipitation route for antibacterial applications. *Nanoparticle Res* 17:57. <https://doi.org/10.1007/s11051-014-2853-9>

**Publisher's Note** Springer Nature remains neutral with regard to jurisdictional claims in published maps and institutional affiliations.